minerals

MDPI

Article

Tectonic Transformation and Metallogenesis of the Yanshan Movement during the Late Jurassic Period: Evidence from Geochemistry and Zircon U-Pb Geochronology of the Adamellites in Xingcheng, Western Liaoning, China

Pengyue Hu [1], Chenyue Liang [1,2,*], Changqing Zheng [1,2], Xiao Zhou [1], Yan Yang [1] and Erlin Zhu [1]

[1] College of Earth Sciences, Jilin University, Changchun, Jilin 130061, China
[2] Key Laboratory of Mineral Resources Evaluation in Northeast Asia, Ministry of Land and Resources, Jilin University, Changchun, Jilin 130061, China
* Correspondence: chenyueliang@jlu.edu.cn; Tel.: +86-1516-4362-972

Received: 31 July 2019; Accepted: 27 August 2019; Published: 28 August 2019

Abstract: The Yanshan Movement occurred mainly during the Middle-Late Jurassic, and gave rise to NE trending structures, magmatic events, volcanism and mineral resources. The transformation and evolution of the movement during the Middle-Late Jurassic were investigated from the rock assemblage, geochemistry, and chronology in adamellites which were exposed in the Xingcheng area, western Liaoning. Two types of adamellites were recognized—biotite adamellites with the formation age of 172–168 Ma and garnet-bearing adamellites of 158–152 Ma. All the samples of the two types of adamellites displayed enriched characteristics with high content of SiO_2 (66.86–75.55 wt.%) and total alkali (Na_2O + K_2O = 7.56–8.71 wt.%), high large ion lithophile element (LILE: K, Rb, Sr), and low high field strength element (HFSE: Ce, Ta, P, Ti). The biotite adamellites belong to metaluminous-peraluminous I-type granites, and show volcanic arc granite characteristics, and were formed by partial melting of the ancient crust in the compressional setting that resulting from the subduction of the Paleo-Pacific plate beneath the north margin of the North China Craton (NCC). The garnet-bearing adamellites are also metaluminous-peraluminous I-type granites, with characteristics of both the compressional and extensional regimes, which were formed at the middle-late stages of the continuing subduction of the Paleo-Pacific plate, while simultaneously, the frontal side of the subduction slab began to roll back, leading to an extensional environment. Combining with regional geophysical studies and our petrological and geochemical studies, we propose that the eastern segment of the northern margin of NCC may have been controlled by the Paleo-Pacific tectonic domain at the latest in the Middle Jurassic, while the initiation of the tectonic regime from a compressional to an extensional environment was during the Late Jurassic (158–152 Ma) as a response of the Yanshan Movement. Simultaneously, geochronological statistics of the ore deposits in western Liaoning show that the Mesozoic endogenetic metalliferous deposits formed in a compressive environment influenced by the subduction of the Paleo-Pacific plate, similar to the magma events in ages, and the magmatism provided the thermodynamic condition and the source of metallogenic hydrothermal fluid for mineralization.

Keywords: magmatic activity; mineralization; Yanshan Movement; Paleo-Pacific plate; North China Craton (NCC)

---

1. Introduction

Since the concept of the Yanshan Movement [1] was first proposed by the renowned Chinese geologist Wong Wenhao in 1926, scholars have carried out a large number of related research [2–5]. There is a consensus that the initiation and development of the Yanshan Movement were associated with coeval oceanic subduction and continental convergence in the Paleo-Pacific [6–8], the ancient Asian Ocean [7,9], and Mongol-Okhotsk [9–12] tectonic domains. Also, the Yanshan Movement represents the transition from the nearly E-W-trending ancient Asian Ocean tectonic domain to the NNE-trending Paleo-Pacific tectonic domain [6–8,13,14], i.e. the transformation from a continental collision tectonic regime to a continental-margin subduction tectonic regime [15]. However, the timing and development of the tectonic evolution have not been well-established. Based on the evidence of magmatic activities, widespread folding and faulting, and the formation of a series of basins, previous studies proposed three views of the initial time of the tectonic transition: Cretaceous [16], Mid-Late Jurassic [8,11,15], and Early Jurassic [7,8].

Intense and frequent magmatic activities control the formation of the gold and metal metallogenesis [14,17–22]. For example, the formation of the large Wulongshan gold deposits and the Meishan polymetallic deposits in Eastern Shandong were genetically related to the acidic magmas [21,23–25], and some gold and REE deposits in Western Shandong were controlled by alkaline magmas [23,25–27]. These ore-controlling magmas might originate from the upper mantle with complicated underplating and hybrid processes [23], and record the tectonic evolution of the Yanshan Movement. In this study, the Xudapu adamellites in Xingcheng area, western Liaoning were investigated in terms of the geochemistry characters, chronology, and petrogenesis to provide constraints on the tectonic transformation of the Jurassic tectonic movements, and to facilitate the understanding of the deep geodynamic mechanism of the Yanshan Movement and Yanshannian magmatism, as well as their relationships with metallogenesis.

2. Geological Setting

The North China Craton (NCC) is one of the oldest Archean cratons in the world [2,29,30]. Affected by the Yanshan Movement, the eastern part of the craton experienced multiple phases of tectonic deformations and magmatic activities in the Mesozoic period [31–35], especially large-scale lithospheric thinning during the Early Cretaceous period [1,8,36–39].

The Xudapu area, south of Xingcheng, Western Liaoning, is located near the northern margin of the East NCC, and is tectonically situated in the transitional region between the Shanhaiguan Uplift and Hebei–Liaoning Subsidence (Figure 1), where the structural trend transformed from N-E trend to NNE direction [40]. Having undergone extensive mobilization and modification and experienced an extremely similar evolution procedure with NCC in the Yanshan period [41,42], the study area experienced an extremely similar evolution procedure with NCC, thus, this area provides an ideal opportunity to study the tectonic evolution of the Yanshan Movement. Previous research has done systematic research work on the Mesozoic granites in western Liaoning, and established a chronological framework for the Mesozoic granitic magmatism in the Xingcheng area [42–46]. Large-scale N-E trending faults in the area were developed, along with a series of metallic deposits such as the Suiquan gold deposit, the Yangjiazhangzi molybdenum deposit, although other ore deposits also occur in NE-SW trending regional structure [17,47]. Various types of Mesozoic intrusive rocks were exposed in the study area, most of which were Late Jurassic granites, and minors formed in Late Triassic and Early Cretaceous (Figure 2). The Neoarchean granitic rocks are exposed in the middle part of the study area among the Mesozoic granites as giant xenoliths, mainly composed of granitic gneiss and biotite-plagioclase gneiss [17,28,48,49]. The Late Triassic and Early Cretaceous rocks are mainly porphyritic granitic gneiss and some light colored dikes of granites, respectively. The Late Jurassic adamellites, which are granites rich in plagioclases and K-feldspars, are the largest intrusive magmatic rocks in the northern and southern sectors of the study area, and some dikes of biotite adamellites intrude the Neoarchean granite gneisses. These rocks show a massive structure in the south and a gneissic structure with shear fabrics in the north [28].

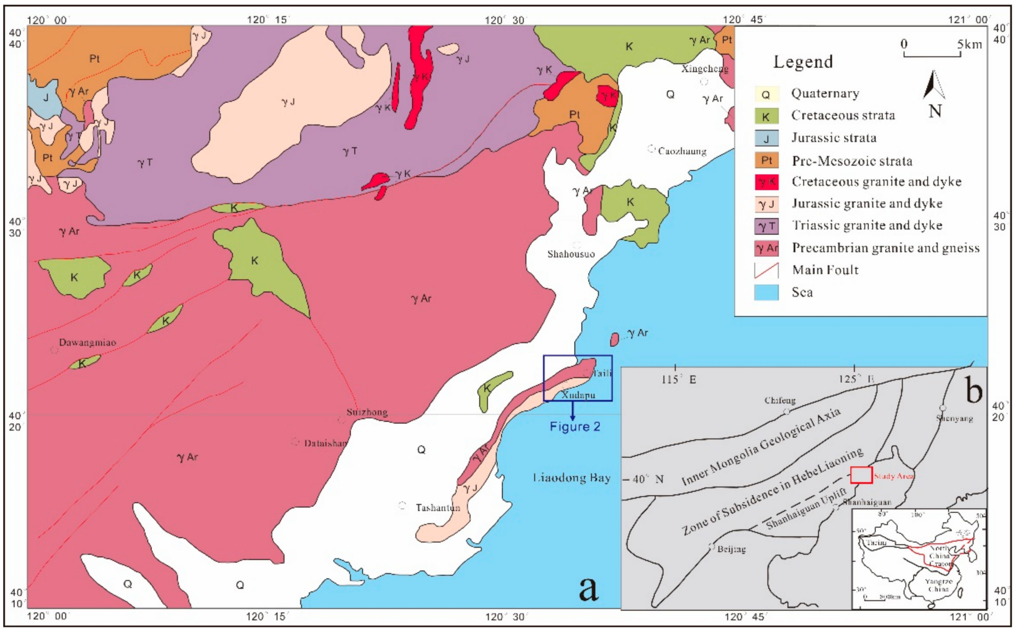

Figure 1. (**a**) Tectonic sketch map of Eastern North China Craton (NCC). (**b**) Simplified geological map of the Xingcheng-Xudapu area at the NE margin of the NCC (modified from Liang et al. [28]).

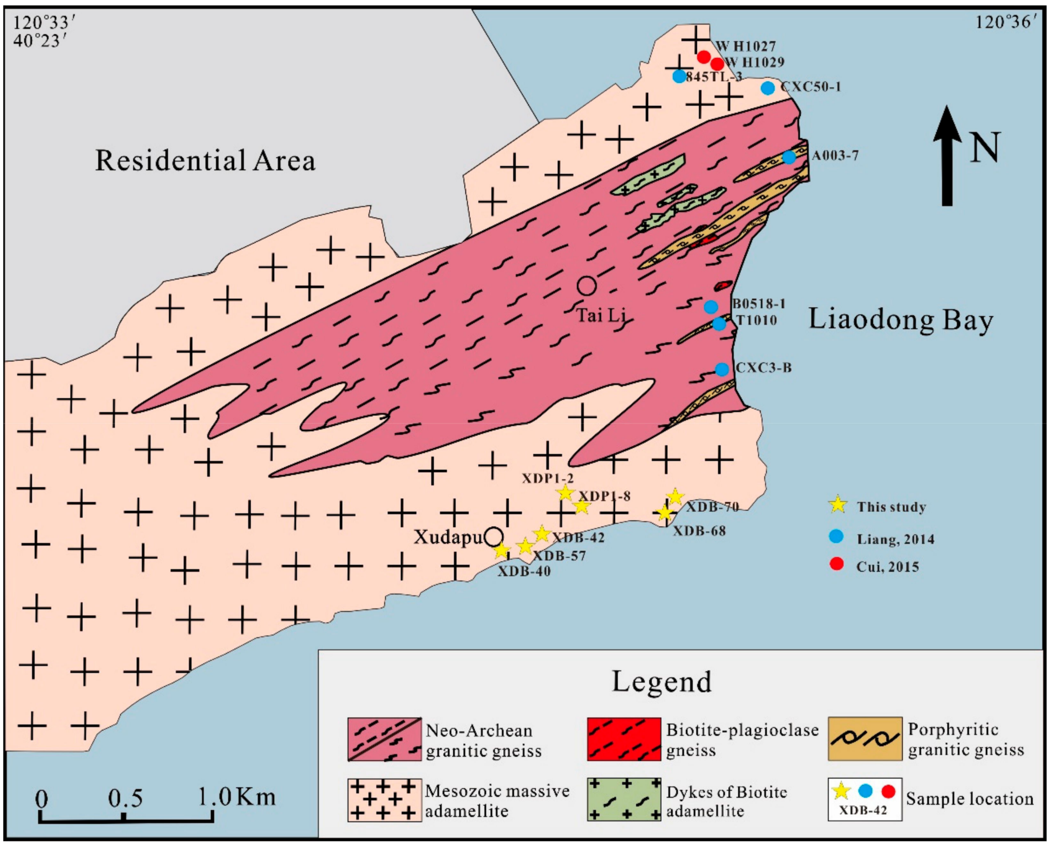

Figure 2. Geological map of the Xingcheng-Xudapu area showing the distribution of various granitic and gneissic rocks with sampling locations.

3. Sampling and Petrography

Samples were collected from the seacoast of Liaodong Bay in the Xudapu area (Figure 2), divided into two main types: Garnet-bearing adamellites and biotite adamellites (Figure 3). Garnet-bearing adamellites are widely exposed in the study area. Typical rocks are mostly grayish-white in hand specimens with massive structures. The garnet grains or garnet aggregates, are present as magmatic grains in adamellites (Figure 3c). The main minerals are plagioclase (~30%), alkali feldspar (~30%), quartz (~32%), biotite (~5%), and garnet (~3%), with accessory titanite, zircon, and apatite. The feldspar grows in multiple stages. A few plagioclases are weakly altered to sericites, but still display visible multiple twins. The alkali feldspar is microcline-perthite with cross-hatched twins and locally forms an intergrowth with quartz. The garnet grains range from 6 to 7 mm with inclusions of quartz and plagioclase inside, which forms a diablastic structure (Figure 3d).

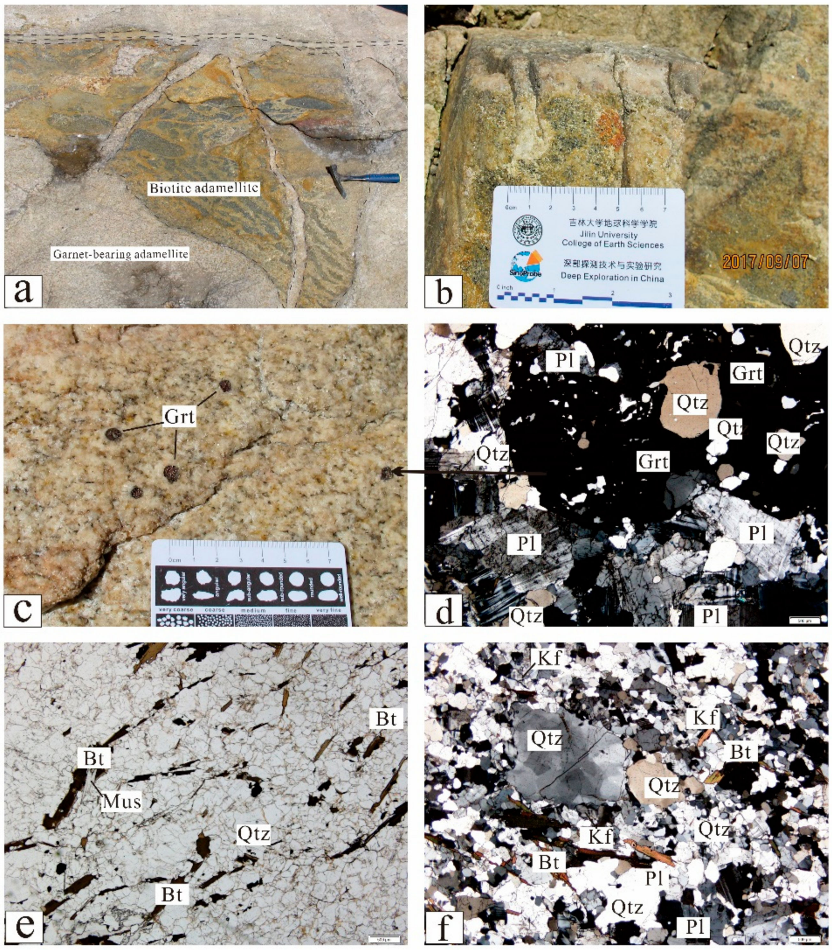

Figure 3. (**a**,**b**) Biotite adamellites are exposed as xenolith in the garnet-bearing adamellites. (**c**) Garnet-bearing adamellites with inclusions of large garnet particles or garnet aggregates. (**d**) The garnet with inclusions of quartz and plagioclase inside. (**e**,**f**) Aligned biotite and elongated recrystallized quartz formed a weakly gneissic texture. Note: Bt-Biotite; Grt-Garnet; Kf-K-feldspar; Mus-Muscovite; Pl-Plagiocase; Qtz-Quartz.

Biotite adamellites are exposed as xenolith in the garnet-bearing adamellites, and they cut the garnet granitic aplite (Figure 3a). The biotite adamellites are yellow-brown in hand specimens (Figure 3b) and consist of quartz (~40%), plagioclase (~25%), alkali feldspar (~20%), biotite (~15%) with accessory ilmenite and apatite. Quartz is elongated, showing recrystallized texture (Figure 3f). Biotite is typically aligned to form a weak gneissic texture, together with elongated quartz, suggesting that the rocks are deformed and foliated. (Figure 3e,f).

4. Analytical Methods

4.1. Major and Trace Elements

Seven representative samples were selected for detailed study. The samples were ground, shrunk, and tested for whole-rock major and trace element analyses in the test center of the First Geological Institute of the China Metallurgical Geology Bureau. Fresh whole-rock samples were ground in an agate mill to less than 200 mesh. The major elements were analyzed on fused glass disks using X-ray fluorescence spectroscopy (XRF, Japan Rigaku) and the trace element analyses were analyzed by inductively coupled plasma mass spectrometry (ICP-MS, America Thermo). Distilled HF + HNO_3 and high pressure sealed Teflon bombs were used to decompose samples. The analytical uncertainties are approximately 1–3%, and analytical results obtained from the international reference materials WBG07103 and WGB07105. The analytical precision for most elements is better than 5%.

4.2. Zircon U-Pb Dating

Four samples from adamellite rocks exposed in the study area were selected for U-Pb zircon dating in order to determine their crystallization ages. Zircons were separated from whole-rock samples by using the combined heavy liquid and magnetic techniques and then underwent handpicking under a binocular microscope at the Langfang Regional Geological Survey, Hebei Province, China. LA–ICP–MS zircon U-Pb analyses were performed using Agilent 7500A inductively coupled plasma mass spectrometer (ICP–MS) equipped with Coherent COM-PExPro 200M 193-nm ArF excimer laser, housed at the Key Laboratory of Mineral Resources Evaluation of Northeast Asia, Ministry of Natural Resources, Jilin University. All measurements were performed using zircon 91500 as an external standard for age calculation. NIST SRM 610 was used as an external standard for measurements of trace element concentrations. The concentrations of U, Th, and Pb elements were calibrated using ^{29}Si as an internal calibrant. $^{207}Pb/^{206}Pb$, $^{206}Pb/^{238}U$ and $^{207}Pb/^{235}U$ ratios and apparent ages were calculated using ICPMSDataCal [50]. The age calculations and concordia plots were made using Isoplot (Ver. 3.0) [51].

5. Results

5.1. Major and Trace Elements

The major and trace element data on all the samples are presented in Table 1. In the TAS classification diagram, all garnet-bearing adamellites plot in the granite field and most of the biotite adamellites plot in the quartz monzonite fields (Figure 4). Biotite adamellites have SiO_2 = 66.86–69.52 wt.%, CaO = 0.84–1.68 wt.%, Fe_2O_3 = 2.39–3.99 wt.%, MgO = 0.77–1.13 wt.%. The $Mg^{\#}$ values of these rocks were relatively low and ranged from 16.8 to 23.6. Garnet-bearing adamellites had relatively high SiO_2 (74.24–75.55 wt.%), and were relatively low in CaO (0.79–0.93 wt.%), Fe_2O_3 (0.03–1.04 wt.%), and MgO (0.10–0.21 wt.%). The $Mg^{\#}$ values (10.5–14.6) were even lower than the biotite adamellites (xenoliths) enclosed in the garnet-bearing adamellites. All the samples were high in $Na_2O + K_2O$ (7.56–8.69 wt.%) and mostly K_2O/Na_2O = 0.59–1.33. Most of them were metaluminous-peralumunous with A/CNK of 0.91–1.05 (Figure 5b), and plot in the high K calc–alkaline series field in the rock series K_2O vs. SiO_2 diagram (Figure 5a), with a high differentiation index (DI = 81.28–94.78).

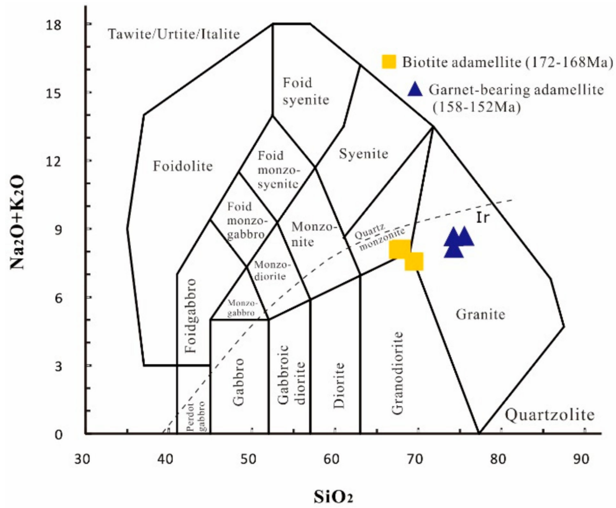

Figure 4. TAS classification diagram of the Xudapu-Xingcheng adamellites. Note: Ir-Irvine boundary line, above is alkaline, below is subalkalic (after [52]).

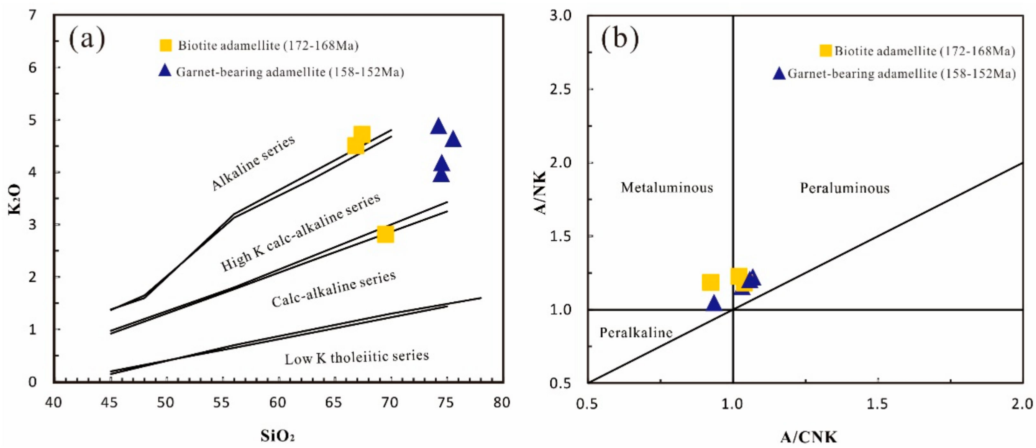

Figure 5. K_2O vs SiO_2 discrimination plots (**a**) and A/NK-A/CNK discrimination plots (**b**) of theadallemites in the Xudapu-Xingcheng area. The boundary lines are from [53] and [54], respectively.

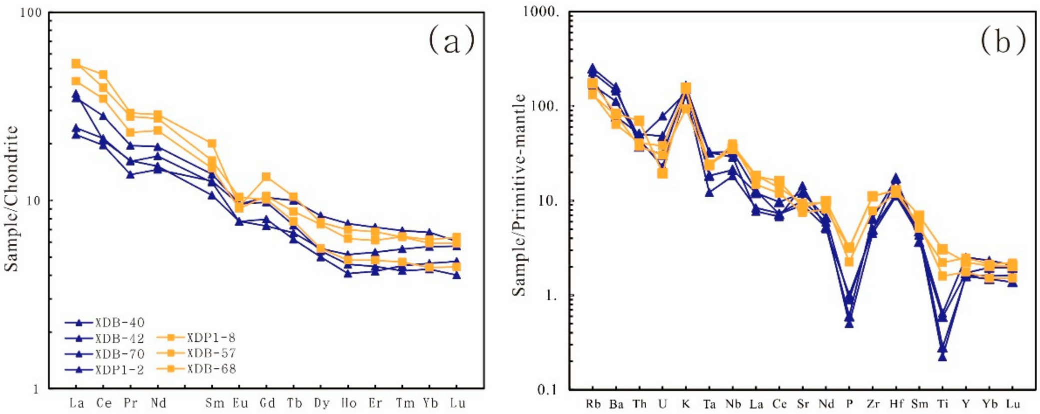

Figure 6. Chondrite-normalized rare earth element (REE) patterns (**a**) and primitive mantle-normalized trace element patterns. (**b**) for the Xudapu-Xingcheng adamellites. Chondrite and primitive mantle data are from Sun and McDonough [55].

The total rare earth element (REE) content of biotite adamellites was relatively low, varying from 54.50 to 68.66 ppm. The $(La/Yb)_N$ ratio reflecting the REE fractionation was medium, from 6.94–12.20, which is in agreement with the LREE/HREE ratio (6.63–9.52), and the biotite adamellites belong to the

LREE-enriched type. The δEu value ranged from 0.55–0.78, showing a moderate negative Eu anomaly. The chondrite-normalized REE patterns were smooth and dip slightly to the right (Figure 6a).

Compared with biotite adamellites, garnet-bearing adamellites had lower REE content (∑REE = 35.62–44.58 ppm), and had similar chondrite-normalized REE patterns with a slight dipping to the right (Figure 6a). They are relatively enriched in light rare earth elements [LREE/HREE = 3.62–6.97 (La/Yb)N = 3.30–8.12], displaying less obvious Eu anomalies (δEu = 0.76–0.86).

In the primitive-mantle-normalized diagram (Figure 6b), both the two types of rocks showed moderate enrichment in large-ion lithophile elements (e.g., K, Rb, and Sr) and had negative Ce, Ta, P, and Ti anomalies.

Table 1. Representative major (wt.%) and trace (ppm) element analyses of the Xudapu-Xingcheng adamellites.

Sample	Garnet-Bearing Adamellite				Biotite Adamellite		
	XDB-40	**XDB-42**	**XDB-70**	**XDP1-2**	**XDP1-8**	**XDB-57**	**XDB-68**
Na_2O	3.79	4.06	4.41	4.41	3.54	4.75	3.81
MgO	0.21	0.10	0.13	0.20	1.13	0.77	0.83
Al_2O_3	13.98	12.30	13.96	13.87	13.39	12.85	13.16
SiO_2	74.24	75.55	74.48	74.52	67.42	69.52	66.86
P_2O_5	0.01	0.02	0.01	0.02	0.07	0.05	0.07
K_2O	4.89	4.65	3.98	4.19	4.72	2.81	4.50
CaO	0.93	0.79	0.89	0.88	1.20	1.68	0.84
TiO_2	0.13	0.06	0.05	0.14	0.66	0.35	0.48
MnO	0.05	0.06	0.05	0.05	0.15	0.12	0.15
TFe_2O_3	2.50	1.62	1.45	1.83	7.58	5.37	8.50
LOI	0.06	0.05	0.22	0.13	0.84	0.94	0.22
Total	100.80	99.26	99.63	100.26	100.69	99.22	99.41
Ba	541	1101	784	1008	580	561	447
Cr	17.9	44.8	26.7	17.6	15.6	14.9	17.9
Nb	23.6	15.1	13.0	20.6	25.2	27.5	28.3
Ni	2.17	1.81	1.61	2.21	7.66	1.58	1.55
Rb	121	160	106	144	111	83.0	85.5
Sr	190	255	211	304	181	199	158
Ta	1.32	0.75	0.50	1.33	0.98	0.99	0.95
Th	4.32	3.16	3.77	3.85	5.94	3.19	3.47
U	1.01	0.64	0.48	1.65	0.41	0.63	0.80
Y	7.81	7.23	7.41	11.4	10.2	8.01	11.3
Zr	72.2	55.4	50.4	53.9	124	87.2	125
La	8.75	8.29	5.76	5.29	12.5	12.7	10.2
Ce	12.8	17.2	13.1	12.0	28.5	24.3	21.2
Pr	1.54	1.86	1.53	1.30	2.76	2.65	2.18
Nd	7.10	9.00	8.03	6.81	13.4	12.7	11.0
Sm	1.63	2.11	1.91	1.94	3.07	2.49	2.27
Eu	0.45	0.56	0.45	0.55	0.54	0.60	0.53
Gd	1.50	2.01	1.63	2.13	2.75	2.08	2.17
Tb	0.25	0.28	0.23	0.37	0.39	0.29	0.33
Dy	1.41	1.37	1.27	2.11	1.94	1.41	1.89
Ho	0.29	0.26	0.23	0.43	0.40	0.27	0.35
Er	0.88	0.74	0.69	1.19	1.13	0.80	1.02
Tm	0.14	0.11	0.11	0.18	0.16	0.12	0.16
Yb	0.97	0.73	0.79	1.15	1.01	0.75	1.05
Lu	0.15	0.10	0.12	0.15	0.15	0.11	0.16

5.2. Geochronology

Cathodoluminescence (CL) images of representative analyzed zircon grains are shown in Figure 7, and the U-Pb-Th isotopic ratios, as well as concentrations of U, Th, and Pb, are given in Table 2.

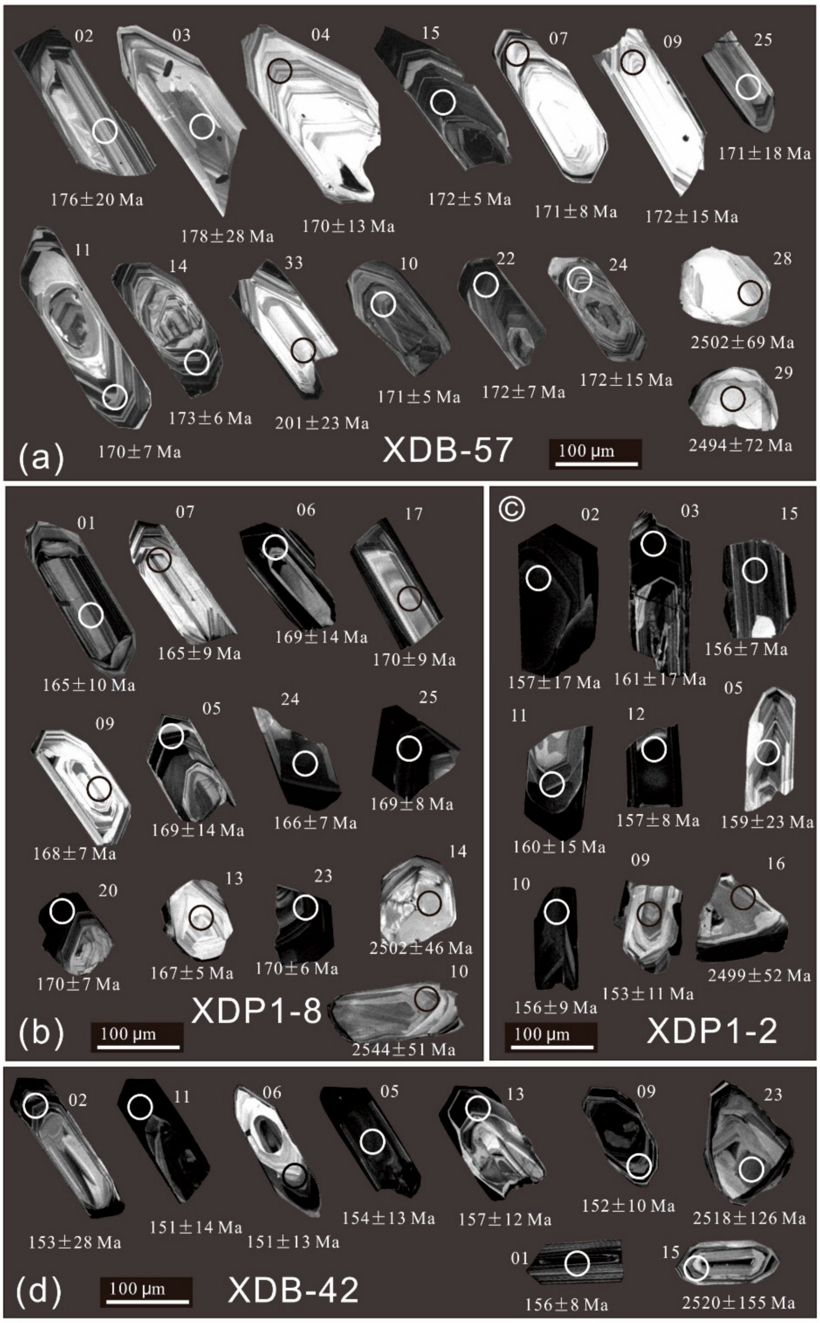

Figure 7. Cathodoluminescence (CL) images of representative zircons from all selected samples. LA–ICP-MS spots and corresponding apparent $^{206}Pb/^{238}U$ ages (Ma) (< 1.0 Ga) or $^{207}Pb/^{206}Pb$ ages (Ma) (> 1.0 Ga) are reported with 1σ uncertainties.

Two biotite adamellites (XDB-57 and XDP1-8) were dated. The zircons were colorless to light yellow, which occurred as short prismatic grains in 100–200 µm diameter, subhedral to euhedral. Most of the grains had well-preserved crystal faces and showed a clear internal oscillatory zoning. Seldom grains from sample XDB-57 and sample XDP1-8 had weakly zoned outer cores, surrounded by a thick overgrowth of euhedrally-zoned zircon with weak or no luminescence (Figure 7a,b). Sample XDB-57 and XDP1-8 give a mean $^{206}Pb/^{238}U$ age, respectively, of 172 ± 2 Ma (MSWD = 0.1, n = 18) and 168 ± 2 Ma (MSWD = 0.3, n = 17) (Figure 8a,b). These dated spots on the concordia curve show diverse Th/U ratios of (0.14 to 1.42) and (0.22 to 2.15), respectively, which are typical for magmatic zircons. We interpret these ages (172–168 Ma) as the crystallization ages of the biotite adamellites. Several concordant old ages from euhedrally-zoned zircons are 2565 to 2466 Ma (Table 2), and show a high

Th/U ratio of (0.52 to 1.88). We interpret these grains as xenocrysts. Some discordant ages probably are disturbed by Pb loss.

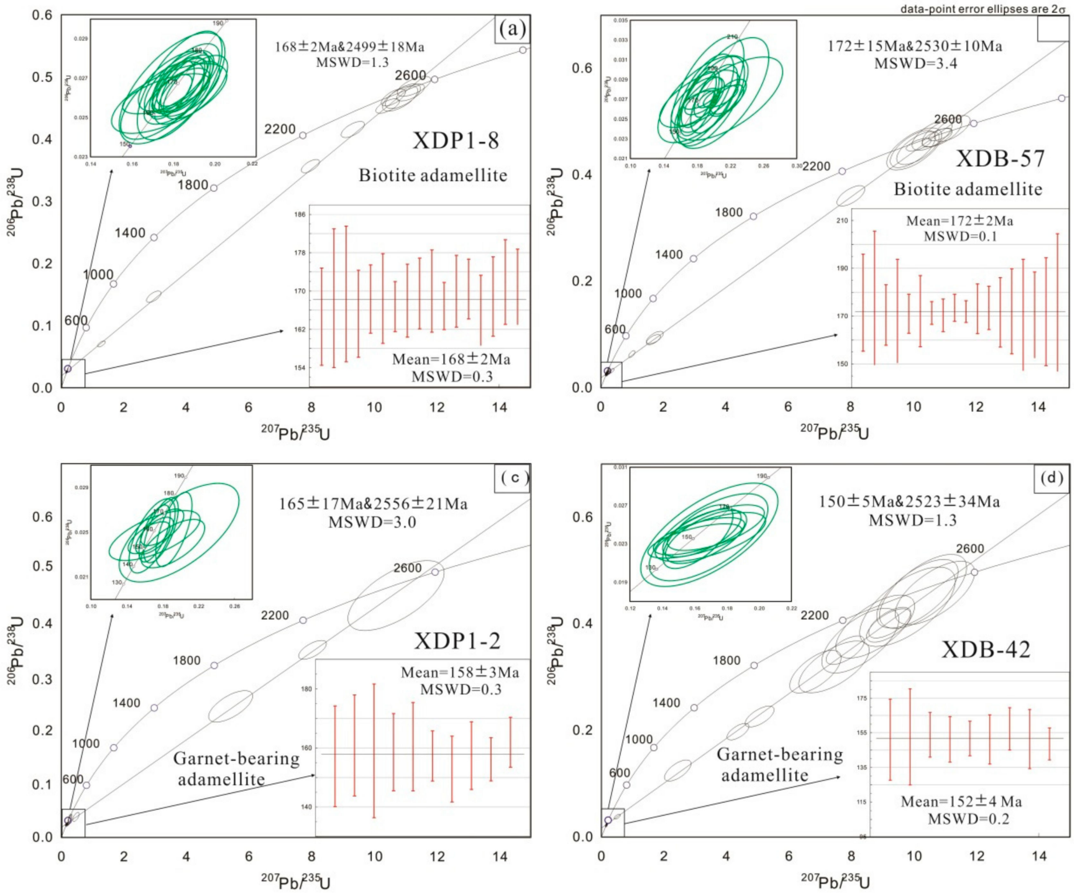

Figure 8. (**a**–**d**) $^{206}Pb/^{238}U$ vs. $^{207}Pb/^{235}U$ concordia plots of all investigated garnet-bearing adamellite and biotite adamellite samples. Errors are 2σ.

41 spots were analyzed from zircons of garnet-bearing adamellites samples XDB-42 and XDP1-2. The zircons were transparent to translucent, subhedral to euhedral, and ranged in size from 80 to 200 µm in diameter. Most of the grains showed obviously or non-evident oscillatory zoning with relatively weakly luminescence (Figure 7c,d). Sample XDB-42 and XDP1-2 give a mean $^{206}Pb/^{238}U$ age, respectively, of 152 ± 4 Ma (MSWD = 0.2, n = 9) and 158 ± 3 Ma (MSWD = 0.3, n = 10), these spots show diverse Th/U ratios of (0.34 to 1.04, except one of 0.05) and (0.34 to 1.30), respectively, indicating their magmatic origin. We interpret these ages (158–152 Ma) as the crystallization ages of the garnet-bearing adamellites. Several concordant old age (2535–2461 Ma, Th/U ratio of (0.36 to 1.36)) from euhedrally-zoned zircons was similarly considered as xenocrysts. The discordant ages recorded multi-stage Pb loss.

Table 2. LA-ICP-MS U-Th-Pb isotopic data of zircons in adamellites from the Xingcheng-Xudapu area.

Spot no.	Concentration (ppm)	Th/U	Isotopic						Ages (Ma)							
	Pb	Th	U		$^{207}Pb/^{206}Pb$	2σ	$^{207}Pb/^{235}U$	2σ	$^{206}Pb/^{238}U$	2σ	$^{207}Pb/^{206}Pb$	2σ	$^{207}Pb/^{235}U$	2σ	$^{206}Pb/^{238}U$	2σ
XDB-42: Garnet-bearong adamellite																
XDB-42-1	13.38	201.34	344.01	0.59	0.0533	0.0087	0.1687	0.0300	0.0237	0.0037	343	333	158	26	151	23
XDB-42-2	24.88	443.89	455.53	0.97	0.0512	0.0060	0.1692	0.0347	0.0240	0.0044	250	248	159	30	153	28
XDB-42-3	241.66	221.15	184.87	1.20	0.1653	0.0111	10.2947	1.1391	0.4610	0.0568	2510	113	2462	102	2444	251
XDB-42-4	413.64	415.91	675.46	0.62	0.1677	0.0103	7.4446	0.9211	0.3193	0.0397	2535	104	2166	111	1786	194
XDB-42-5	17.45	253.56	310.37	0.82	0.0481	0.0046	0.1646	0.0198	0.0241	0.0020	106	217	155	17	154	13
XDB-42-6	10.04	123.46	224.20	0.55	0.0496	0.0068	0.1699	0.0279	0.0237	0.0021	176	302	159	24	151	13
XDB-42-7	109.50	68.88	152.58	0.45	0.1605	0.0067	9.2238	0.5493	0.4024	0.0235	2461	72	2360	55	2180	108
XDB-42-8	21.84	56.82	158.76	0.36	0.1289	0.0086	2.4443	0.3473	0.1249	0.0163	2083	117	1256	102	759	93
XDB-42-9	11.12	125.13	332.74	0.38	0.0482	0.0060	0.1628	0.0231	0.0238	0.0016	109	280	153	20	152	10
XDB-42-10	316.17	290.84	406.76	0.72	0.1546	0.0074	7.8052	0.5008	0.3506	0.0219	2398	82	2209	58	1938	104
XDB-42-11	97.17	1392.25	2360.21	0.59	0.0487	0.0041	0.1672	0.0205	0.0237	0.0023	132	185	157	18	151	14
XDB-42-12	554.28	607.64	509.23	1.19	0.1545	0.0087	5.0648	0.3793	0.2262	0.0160	2398	101	1830	64	1314	84
XDB-42-13	23.33	221.70	643.46	0.34	0.0481	0.0053	0.1732	0.0246	0.0247	0.0019	102	244	162	21	157	12
XDB-42-14	197.35	151.49	304.79	0.50	0.1623	0.0130	8.2867	1.0087	0.3686	0.0496	2480	135	2263	110	2023	234
XDB-42-15	72.70	55.23	90.04	0.61	0.1661	0.0153	9.7977	1.2491	0.4321	0.0609	2520	155	2416	117	2315	274
XDB-42-16	268.70	274.78	133.08	2.06	0.1616	0.0142	10.1123	1.0642	0.4566	0.0527	2473	149	2445	97	2424	233
XDB-42-17	218.59	217.83	337.62	0.65	0.1591	0.0117	6.8481	0.6721	0.3104	0.0328	2447	125	2092	87	1743	161
XDB-42-18	121.53	106.63	110.06	0.97	0.1572	0.0103	8.7629	1.0285	0.3950	0.0483	2428	145	2314	107	2146	223
XDB-42-19	26.18	91.79	1735.04	0.05	0.0487	0.0050	0.1621	0.0178	0.0238	0.0027	132	235	153	16	151	17
XDB-42-20	41.59	560.91	418.87	1.34	0.0855	0.0079	0.5070	0.0803	0.0384	0.0038	1328	180	416	54	243	23
XDB-42-21	29.45	475.83	457.64	1.04	0.0479	0.0067	0.1602	0.0237	0.0233	0.0015	100	294	151	21	149	9
XDB-42-22	166.69	101.45	223.04	0.45	0.1605	0.0079	9.1956	0.5810	0.3970	0.0256	2461	83	2358	58	2155	118
XDB-42-23	211.80	185.42	136.70	1.36	0.1660	0.0125	10.6747	1.0400	0.4581	0.0486	2518	126	2495	90	2431	215
XDB-42-24	114.41	69.94	393.61	0.18	0.1515	0.0069	4.3710	0.2888	0.1978	0.0127	2363	78	1707	55	1163	68
XDB-57: Biotite adamellite																
XDB-57-1	91.55	1803.96	1590.17	1.13	0.0559	0.0051	0.2300	0.0264	0.0323	0.0047	456	204	210	22	205	29
XDB-57-2	6.78	90.05	141.25	0.64	0.0539	0.0137	0.1906	0.0275	0.0276	0.0032	369	485	177	23	176	20
XDB-57-3	5.60	138.72	97.70	1.42	0.0597	0.0107	0.1927	0.0358	0.0279	0.0045	591	396	179	30	178	28
XDB-57-4	4.25	79.09	83.15	0.95	0.0508	0.0068	0.1811	0.0261	0.0268	0.0020	232	285	169	22	170	13
XDB-57-5	158.94	201.48	159.03	1.27	0.1648	0.0059	10.1573	0.5608	0.4506	0.0253	2506	60	2449	51	2398	113
XDB-57-6	4.19	57.46	84.98	0.68	0.0637	0.0188	0.2182	0.0530	0.0271	0.0034	731	526	200	44	172	22
XDB-57-7	18.08	91.05	509.71	0.18	0.0582	0.0040	0.2157	0.0167	0.0269	0.0013	539	147	198	14	171	8
XDB-57-8	212.34	335.46	178.14	1.88	0.1632	0.0054	10.6067	0.5219	0.4746	0.0229	2500	56	2489	46	2504	100
XDB-57-9	2.34	48.88	41.15	1.19	0.0512	0.0099	0.1833	0.0393	0.0271	0.0024	256	383	171	34	172	15

Table 2. *Cont.*

Spot no.	Concentration (ppm)	Th/U	Isotopic								Ages (Ma)					
	Pb	Th	U		^{207}Pb/^{206}Pb	2σ	^{207}Pb/^{235}U	2σ	^{206}Pb/^{238}U	2σ	^{207}Pb/^{206}Pb	2σ	^{207}Pb/^{235}U	2σ	^{206}Pb/^{238}U	2σ
XDB-57-10	12.91	148.75	314.54	0.47	0.0490	0.0038	0.1829	0.0155	0.0269	0.0008	146	174	171	13	171	5
XDB-57-11	12.84	131.12	346.32	0.38	0.0509	0.0043	0.1866	0.0172	0.0268	0.0011	235	194	174	15	170	7
XDB-57-12	260.43	372.20	216.23	1.72	0.1611	0.0043	10.1773	0.3271	0.4571	0.0098	2478	45	2451	30	2427	43
XDB-57-13	207.84	192.08	218.42	0.88	0.1651	0.0038	10.8684	0.3051	0.4761	0.0097	2508	39	2512	26	2510	42
XDB-57-14	25.73	211.87	662.80	0.32	0.0553	0.0043	0.2086	0.0169	0.0273	0.0009	433	176	192	14	173	6
XDB-57-15	35.75	650.61	745.87	0.87	0.0521	0.0027	0.1939	0.0103	0.0270	0.0007	287	149	180	9	172	5
XDB-57-16	69.92	1064.94	1485.85	0.72	0.0517	0.0027	0.1935	0.0137	0.0272	0.0017	272	119	180	12	173	10
XDB-57-17	142.94	134.17	154.25	0.87	0.1658	0.0044	10.7643	0.3933	0.4701	0.0142	2517	44	2503	34	2484	62
XDB-57-18	265.18	144.20	482.98	0.30	0.1611	0.0052	8.0070	0.3660	0.3608	0.0157	2478	54	2232	41	1986	74
XDB-57-19	145.04	372.54	1082.84	0.34	0.1319	0.0065	1.6847	0.1827	0.0907	0.0078	2124	86	1003	69	560	46
XDB-57-20	115.02	110.25	115.38	0.96	0.1663	0.0056	10.9239	0.5191	0.4798	0.0220	2520	56	2517	44	2526	96
XDB-57-21	24.39	636.05	393.84	1.61	0.0586	0.0040	0.2180	0.0175	0.0273	0.0014	550	150	200	15	173	9
XDB-57-22	44.72	989.59	809.68	1.22	0.0498	0.0033	0.1823	0.0172	0.0270	0.0023	187	149	170	15	172	15
XDB-57-23	38.24	891.60	658.07	1.35	0.0547	0.0047	0.2007	0.0231	0.0270	0.0028	398	197	186	20	172	18
XDB-57-24	24.03	168.18	627.70	0.27	0.0528	0.0041	0.1967	0.0331	0.0268	0.0037	320	150	182	28	171	23
XDB-57-25	29.07	397.00	686.77	0.58	0.0509	0.0041	0.1831	0.0194	0.0268	0.0029	239	185	171	17	171	18
XDB-57-26	16.50	250.96	407.83	0.62	0.0499	0.0087	0.1874	0.0442	0.0270	0.0036	191	359	174	38	172	23
XDB-57-27	9.70	109.77	208.10	0.53	0.0540	0.0072	0.2113	0.0450	0.0276	0.0046	372	306	195	38	176	29
XDB-57-28	101.61	107.79	113.11	0.95	0.1643	0.0067	9.9926	0.5924	0.4487	0.0284	2502	69	2434	55	2390	127
XDB-57-29	85.08	75.94	101.08	0.75	0.1636	0.0070	10.0360	0.7196	0.4488	0.0323	2494	72	2438	66	2390	144
XDB-57-30	39.37	58.38	417.68	0.14	0.1143	0.0045	0.9922	0.0811	0.0635	0.0053	1933	71	700	41	397	32
XDB-57-31	31.38	308.14	589.64	0.52	0.0526	0.0034	0.2491	0.0213	0.0352	0.0032	322	142	226	17	223	20
XDB-57-32	208.03	174.13	226.81	0.77	0.1663	0.0055	11.2513	0.4687	0.4873	0.0199	2521	56	2544	39	2559	86
XDB-57-33	9.95	146.06	235.19	0.62	0.0734	0.0140	0.3295	0.0783	0.0317	0.0037	1026	394	289	60	201	23
XDB-57-34	73.51	1121.09	1395.66	0.80	0.0700	0.0036	0.3066	0.0203	0.0313	0.0013	931	106	272	16	199	8
XDB-57-35	111.35	196.15	737.01	0.27	0.1264	0.0070	1.7308	0.2195	0.0946	0.0095	2048	98	1020	82	583	56
XDP1-2: Garnet-bearong adamellite																
XDP1-2-1	41.96	743.41	962.19	0.77	0.0601	0.0069	0.2632	0.0402	0.0361	0.0064	606	245	237	32	229	40
XDP1-2-2	48.66	451.90	1322.13	0.34	0.0491	0.0036	0.1684	0.0210	0.0247	0.0027	154	163	158	18	157	17
XDP1-2-3	135.50	3221.46	2574.52	1.25	0.0561	0.0032	0.1926	0.0165	0.0253	0.0027	457	132	179	14	161	17
XDP1-2-4	493.65	278.65	771.51	0.36	0.1723	0.0099	10.6937	1.2569	0.4530	0.0536	2580	96	2497	109	2409	238
XDP1-2-5	8.23	269.39	185.87	1.45	0.0582	0.0153	0.1984	0.0545	0.0250	0.0036	539	490	184	46	159	23
XDP1-2-6	141.30	3291.92	2997.93	1.10	0.0500	0.0025	0.1711	0.0143	0.0249	0.0021	195	113	160	12	159	13
XDP1-2-7	49.33	294.86	1163.53	0.25	0.1054	0.0167	0.4698	0.0851	0.0385	0.0070	1721	295	391	59	244	44
XDP1-2-8	146.26	3119.42	2960.07	1.05	0.0653	0.0077	0.2896	0.0439	0.0362	0.0062	783	246	258	35	230	38
XDP1-2-9	9.25	191.52	191.32	1.00	0.0572	0.0090	0.1915	0.0290	0.0240	0.0018	498	352	178	25	153	11

Table 2. *Cont.*

Spot no.	Concentration (ppm)	Th/U	Isotopic								Ages (Ma)					
	Pb	Th	U		$^{207}Pb/^{206}Pb$	2σ	$^{207}Pb/^{235}U$	2σ	$^{206}Pb/^{238}U$	2σ	$^{207}Pb/^{206}Pb$	2σ	$^{207}Pb/^{235}U$	2σ	$^{206}Pb/^{238}U$	2σ
XDP1-2-10	12.64	242.65	302.28	0.80	0.0690	0.0065	0.2331	0.0198	0.0245	0.0014	898	191	213	16	156	9
XDP1-2-11	35.51	909.72	765.10	1.19	0.0520	0.0032	0.1781	0.0158	0.0252	0.0024	287	141	166	14	160	15
XDP1-2-12	14.85	258.30	332.60	0.78	0.0503	0.0050	0.1711	0.0173	0.0247	0.0013	206	228	160	15	157	8
XDP1-2-13	387.27	235.95	1059.41	0.22	0.1523	0.0067	5.4091	0.5751	0.2456	0.0241	2371	81	1886	91	1416	124
XDP1-2-14	48.31	310.47	788.52	0.39	0.0496	0.0117	0.1711	0.0413	0.0247	0.0018	172	478	160	36	157	11
XDP1-2-15	17.03	371.61	403.35	0.92	0.0485	0.0056	0.1649	0.0191	0.0245	0.0012	124	252	155	17	156	7
XDP1-2-16	137.28	157.05	223.05	0.70	0.1642	0.0051	8.0275	0.3636	0.3514	0.0145	2499	52	2234	41	1941	69
XDP1-2-17	17.01	418.32	321.15	1.30	0.0513	0.0055	0.1796	0.0196	0.0255	0.0013	257	226	168	17	162	8
XDP1-8: Biotite adamellite																
XDP1-8-1	20.47	133.53	616.34	0.22	0.0490	0.0029	0.1748	0.0165	0.0259	0.0016	150	−58	164	14	165	10
XDP1-8-2	107.03	658.77	755.55	0.87	0.1285	0.0050	1.2893	0.1007	0.0714	0.0039	2080	69	841	45	445	24
XDP1-8-3	124.15	134.83	178.67	0.75	0.1614	0.0044	7.9683	0.2393	0.3574	0.0087	2472	46	2227	27	1970	42
XDP1-8-4	40.41	70.79	170.63	0.41	0.1445	0.0051	2.9636	0.1903	0.1474	0.0075	2283	61	1398	49	886	42
XDP1-8-5	23.37	538.47	487.44	1.10	0.0494	0.0038	0.1794	0.0208	0.0265	0.0023	165	180	168	18	169	14
XDP1-8-6	25.80	494.83	563.99	0.88	0.0510	0.0038	0.1830	0.0167	0.0266	0.0023	243	174	171	14	169	14
XDP1-8-7	5.85	109.10	124.45	0.88	0.0503	0.0064	0.1780	0.0227	0.0260	0.0014	206	270	166	20	165	9
XDP1-8-8	137.27	170.78	132.38	1.29	0.1689	0.0059	10.8360	0.4624	0.4661	0.0166	2547	59	2509	40	2466	73
XDP1-8-9	135.39	2337.07	2600.60	0.90	0.0512	0.0021	0.1878	0.0120	0.0265	0.0011	250	98	175	10	168	7
XDP1-8-10	156.48	133.95	174.03	0.77	0.1686	0.0050	10.9238	0.4576	0.4697	0.0162	2544	51	2517	39	2482	71
XDP1-8-11	105.98	87.40	125.40	0.70	0.1665	0.0042	10.4371	0.3079	0.4541	0.0095	2524	42	2474	27	2413	42
XDP1-8-12	219.66	5400.12	3388.38	1.59	0.0506	0.0028	0.1843	0.0111	0.0265	0.0015	233	123	172	10	168	9
XDP1-8-13	8.07	102.43	190.14	0.54	0.0488	0.0048	0.1765	0.0172	0.0262	0.0008	200	154	165	15	167	5
XDP1-8-14	85.45	53.89	104.19	0.52	0.1643	0.0045	10.6197	0.3154	0.4678	0.0112	2502	46	2490	28	2474	49
XDP1-8-15	185.19	4012.65	3074.00	1.31	0.0492	0.0021	0.1792	0.0089	0.0264	0.0012	167	100	167	8	168	8
XDP1-8-16	169.13	3506.06	2926.37	1.20	0.0494	0.0018	0.1826	0.0103	0.0266	0.0012	169	89	170	9	169	7
XDP1-8-17	32.58	527.66	761.72	0.69	0.0497	0.0034	0.1828	0.0137	0.0267	0.0014	189	159	170	12	170	9
XDP1-8-18	21.61	250.31	476.70	0.53	0.0487	0.0030	0.2139	0.0142	0.0319	0.0012	200	72	197	12	203	8
XDP1-8-19	217.31	5004.67	3632.50	1.38	0.0495	0.0019	0.1793	0.0079	0.0262	0.0008	172	89	167	7	167	5
XDP1-8-20	57.54	1293.48	1076.34	1.20	0.0508	0.0024	0.1865	0.0104	0.0267	0.0012	232	111	174	9	170	7
XDP1-8-21	110.19	152.36	90.61	1.68	0.1707	0.0050	11.1700	0.3650	0.4757	0.0111	2565	49	2537	31	2508	48
XDP1-8-22	42.17	46.68	39.91	1.17	0.1684	0.0050	11.2797	0.4381	0.4857	0.0132	2542	49	2547	36	2552	57
XDP1-8-23	121.77	2694.34	2078.85	1.30	0.0498	0.0021	0.1841	0.0100	0.0268	0.0010	187	100	172	9	170	6
XDP1-8-24	57.18	1659.50	773.61	2.15	0.0503	0.0026	0.1818	0.0130	0.0261	0.0012	209	119	170	11	166	7
XDP1-8-25	94.68	1785.88	1894.34	0.94	0.0520	0.0023	0.1907	0.0126	0.0265	0.0013	283	97	177	11	169	8
XDP1-8-26	300.20	226.00	420.65	0.54	0.1619	0.0042	9.3246	0.3050	0.4163	0.0106	2476	45	2370	30	2244	48
XDP1-8-27	27.10	365.81	726.51	0.50	0.0498	0.0024	0.1861	0.0132	0.0270	0.0014	187	108	173	11	172	9
XDP1-8-28	53.40	1124.93	1060.92	1.06	0.0484	0.0035	0.1802	0.0139	0.0269	0.0013	120	163	168	12	171	8

6. Discussion

6.1. Petrogenesis of Xudapu Adamellites

The geochemical studies show that the biotite adamellite in the study area has a high silica and potassium contents, with moderate contents of REE, relatively rich LREE and moderately negative Eu anomaly, indicating the crustal source of magma. All the samples of biotite adamellites plot in the I-type granite field in the granite Nb vs SiO_2 discriminant diagram (Figure 9a) and the TFeOt/MgO vs Zr+Nb+Ce+Y diagram (Figure 9b), also providing similar evidence. The garnet-bearing adamellites have a similar trend of normalization curve compared to the biotite adamellites, with relatively rich LREE and moderately negative Eu anomaly. Although the garnet and the muscovite are more likely to appear in S-type granites, they are not effective marks for identifying S-type granites [56–68]. Combined with the A/CNK value less than 1.1 (A/CNK = 0.90–1.05) and the corundum content less than 1% (C = 0–0.78), we believe that the garnet-bearing adamellite is not an I-type granite. Also, the garnet-bearing adamellites samples plot in the I-type granite field in the TFeOt/MgO vs. the Zr+Nb+Ce+Y diagram (Figure 9b), while they are located in A-type granite field in the granite Nb vs. SiO_2 discriminant diagram (Figure 9a). We calculate zircon saturation temperatures of garnet-bearing adamellites and biotite adamellites to inverse the temperature in the magma source. The result indicated that the zircon saturation temperatures for garnet-bearing adamellites range in 787–804 °C, the average is 797 °C, and the zircon saturation temperatures for biotite adamellites range 779–785 °C, the average is 781 °C. The temperatures (< 850 °C) suggested that both of them are not A-type granites, thus the garnet-bearing adamellite should be highly fractional I-type granite with part characteristics of type A, and the primary magma may come from the partial melting of the deep crust.

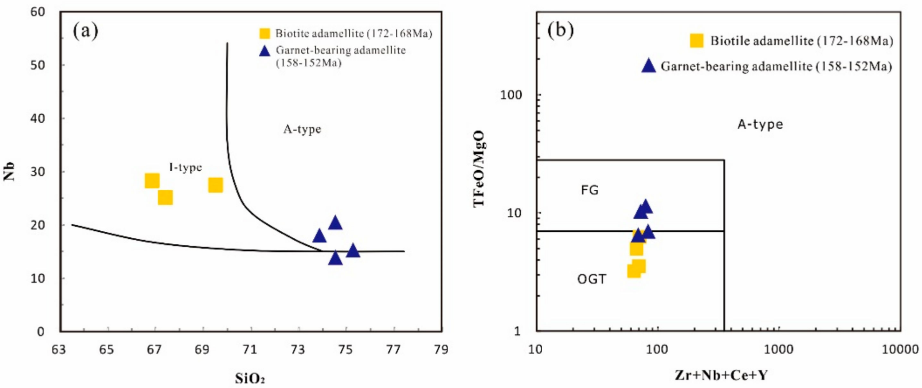

Figure 9. Nb vs. SiO_2 discrimination diagram (**a**) and TFeOt/MgO vs. Zr+Nb+Ce+Y discrimination diagram (**b**) of A-type and I- type granite. The boundary lines are from [59] and [60], respectively.

We compared the REE and trace element data of garnet-bearing adamellites and biotite adamellites in the Xudapu-Xingcheng area with the characteristics of the Mesozoic granites (WH1027, EH1029) studied by [42] in the Taili area (Figure 2), and results show that their distribution patterns have a similar trend (Figure 10). According to [42], the Late Jurassic rocks in the Taili area have negative εHf(t) and ancient crustal T_{DM2} values which indicate the primary magma is from the partial melting of the ancient crust. Thus, we propose that the Late-Middle Jurassic adamellites in the Xingcheng-Xudapu area are mostly consistent with the origin of the partial melting of Neoarchean crust. Some data available on the rare element from the biotite adamellites plot on the discriminant geodynamic diagram suggest that they were formed in a continental margin setting (Figure 11). Combined with the regional geological setting as well as the geochemical characteristics, the biotite adamellites in the Xingcheng-Xudapu area formed in the compressional environment of the subduction of the Paleo-Pacific plate. Similarly, the garnet-bearing adamellites plot in the VAG field closer to the syn-COLG field, and were also formed in the setting of the active continental margin of subduction of Paleo-Pacific plate. Taking the part of characteristics of A-type granite together with the regional geological setting, we propose that they may have been formed mainly in compressional condition, accompanied with sectional extensional characteristics.

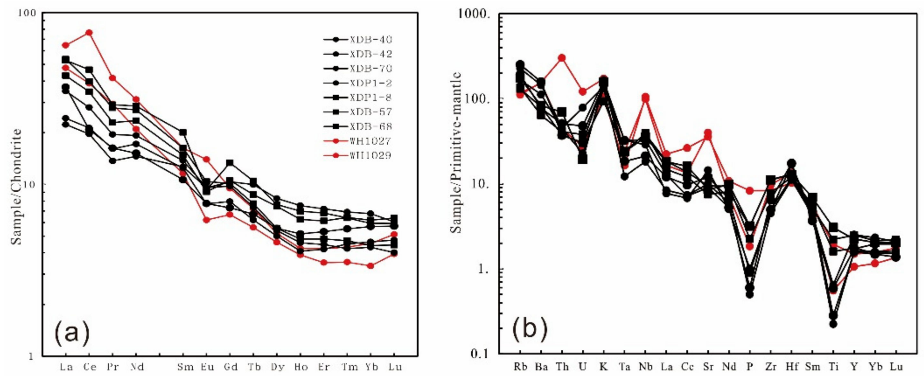

Figure 10. Comparision of chondrite-normalized REE patterns (**a**) and primitive mantle-normalized trace element patterns (**b**) from the Xingcheng-Xudapu adamellites and Mesozoic granites in surrouding area [42]. Chondrite and primitive mantle data are from [55].

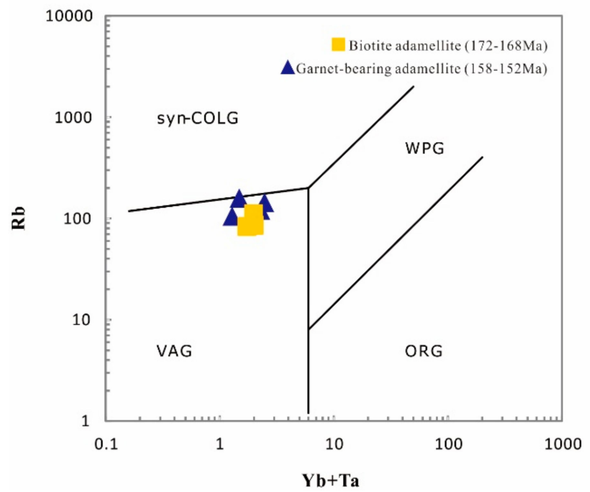

Figure 11. Rb-Yb+Ta discrimination plots of the Xingcheng-Xudapu adamellites. The base map is from [61]. Note: VAG. Volcanic arc granite; WPG. Within-plate granite; Syn-COLG. Syn-collision granite; ORG. Oceanic ridge granite.

6.2. Magmatic Activitives and Tectonic Evolution of the Eastern Segment of NCC during the Middle-Late Jurassic

Our model for the generation and the tectonic setting of the Middle-Late Jurassic granites is as follows (Figure 12). Based on the regional structure characteristics as well as the assemblages of magmatic rocks and their geochemical features, various studies have suggested that the eastern segment of the northern margin of the NCC was in the tectonic setting of the subduction of the Paleo-Pacific plate beneath the NCC during the Middle Jurassic [17,28,62–64]. Liquid was separated from the heated subduction slab, and replaced the superjacent lithospheric mantle, leading to a lower fusible point of the latter. The superjacent lithospheric mantle was partly melted and produced mantle-derived magma, which heated the ancient crust and caused its partly melting [35,65,66]. Continuing dehydration and metasomatism of the subduction slab resulting from the persistent subduction of the Paleo-Pacific plate changed the physical and chemical properties of the lithospheric mantle [42]. The limpen original lithospheric rocks were taken away by asthenospheric mantle, resulting in the thinning of the lithosphere, simultaneously the frontal side of the subduction slab began to roll back [28], leading of an extensional environment.

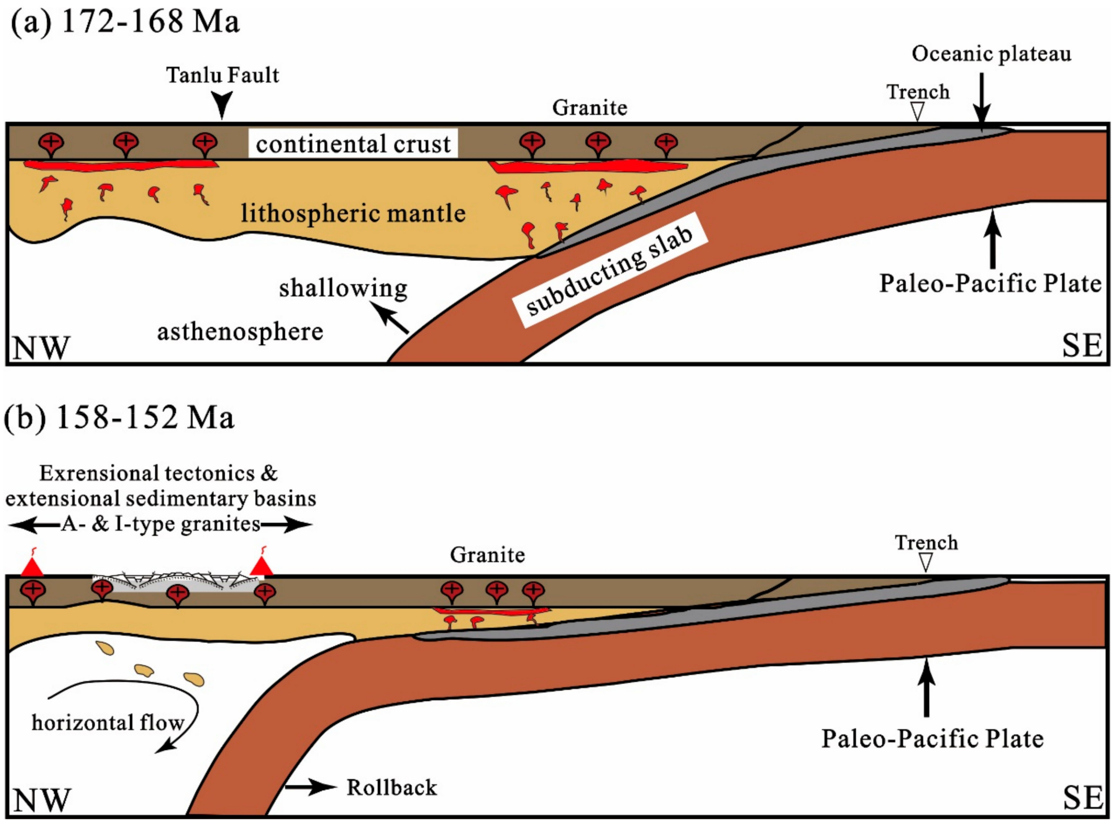

Figure 12. Schematic NW-trending cross-sections from the ancient deep sea-trench of SW Japan to the Yanshan Fold Belt during the Middle-Late Jurassic showing temporal changes in the subducting slab geometry of the tectonic regime and the magmatic episodes. Figures are modified after [28].

There are few records of the metamorphic core complexes or the extensional deformation in Xingcheng-Xudapu area during the Middle Jurassic [39], while voluminous Late Jurassic metamorphic core complexes, as well as extensional sedimentary basins, spread widely in western Liaoning [17,47,67–71], which indicate the extensional structures [34,35,72]. For example, Xu et al. [73] found the Late Jurassic gneissic granite in the eastern part of the NCC, in which the interstitial materials developed directionally, and pointed out that the rocks were formed in the apotectonic and extensional setting. Also, Liang et al. [28] reported the mylonitic granitic belt in Xingcheng, western Liaoning. In addition, the regional geological data show that the ages of 130 to 120 Ma and 160 to 150 Ma were two distinct peak periods for the development of the metamorphic core complexes in the NCC (Figure 13) [8]. In this study, we propose that the tectonic setting began to alter from a compressional to an extensional environment during the Late Jurassic (158–152 Ma).

6.3. The Causal Link between the Large-Scale Mineralization and the Magmatism as well as Yanshan Movement

Large volumes of previous studies have shown that the main metalliferous deposits are distributed along with the N-E metallogenic belts: The Bajiazi–Yangjiazhangzi magmatic-hydrothermal nonferrous polymetallic metallogenic belt and the Qinglong-Huludao volcanic hydrothermal Au-Cu metallogenic belt, and the N-W metallogenic sub-belts between the two N-E metallogenic belts (Figure 13) [90]. The N-E trending metallogenic belts are located between two deep faults of Lugou–Nuerhe and Qinglong–Huludao, with a strata of Neoproterozoic–Early Palaeozoic shallow marine carbonates and clastic rocks. Main gold and molybdenum deposits such as the Suiquan gold deposit and the Yangjiazhangzi molybdenum deposit, some small iron ore spots and the endogenetic metalliferous deposits are distributed in the interior of the magmatic rocks, and the contact zones [90]. The fault can provide the space for magmatism and magma formation, as well as a favorable space for the migration and enrichment of ore-bearing hydrothermal fluid. Also, the granitic magma related to mineralization is of high emplacement without eruption, so that the volatile and the metallogenic elements are well preserved to form the large-scale mineralization in the region. Thus, the fault clefts are always constructions of ore-conducting and ore-bearing structures and in a condition of formation of deposits or ore-bodies [22,23,77,90]. For example, the Wulong Gold Mine in Liaoning province was affected by the Yanshanian tectonic-magmatic. Driven by magmatic thermodynamic forces, the metallogenic material in ancient geological bodies activated, migrated, concentrated, and finally located in granitic gneisses, and then formed the hydrothermal deposit [85]. We investigated the geochronological ages from Mesozoic deposits and magmatic rocks exposed in western Liaoning to determine the association between the Yanshan Movement and mineralization [17,28,44,46,74–89]. Table 3 summarizes the results of the numerical age data of magmatic rocks and deposits from the western Liaoning. Frequency diagrams of compiled geochronological ages (Figure 14) show that the magmatic rocks formed by multistage magmatism during the Mesozoic, overlapping the ages of major metalliferous deposits. This spatiotemporal consistency indicates a possible relationship between the formation of gold, molybdenum deposits, and magmatism in the north of the NCC, the magmatism likely provides the thermodynamic condition and the source of metallogenic hydrothermal fluid for mineralization [21–23,91]. Combined with previous research results, it has been shown that the Mesozoic endogenetic metalliferous deposits formed in a compressive environment influenced by the subduction of the Paleo-Pacific plate similar to the magma events in the north of the NCC [80,83,92,93]. As a more regional perspective, the growth of the large-scale deposits likely coincides in time with the Jurassic reaction and Yanshan Movement affected by the subduction of the Paleo-Pacific plate, and the related magmatic rocks, as well as its surrounding areas, are favorable prospecting targets for endogenetic metalliferous deposits.

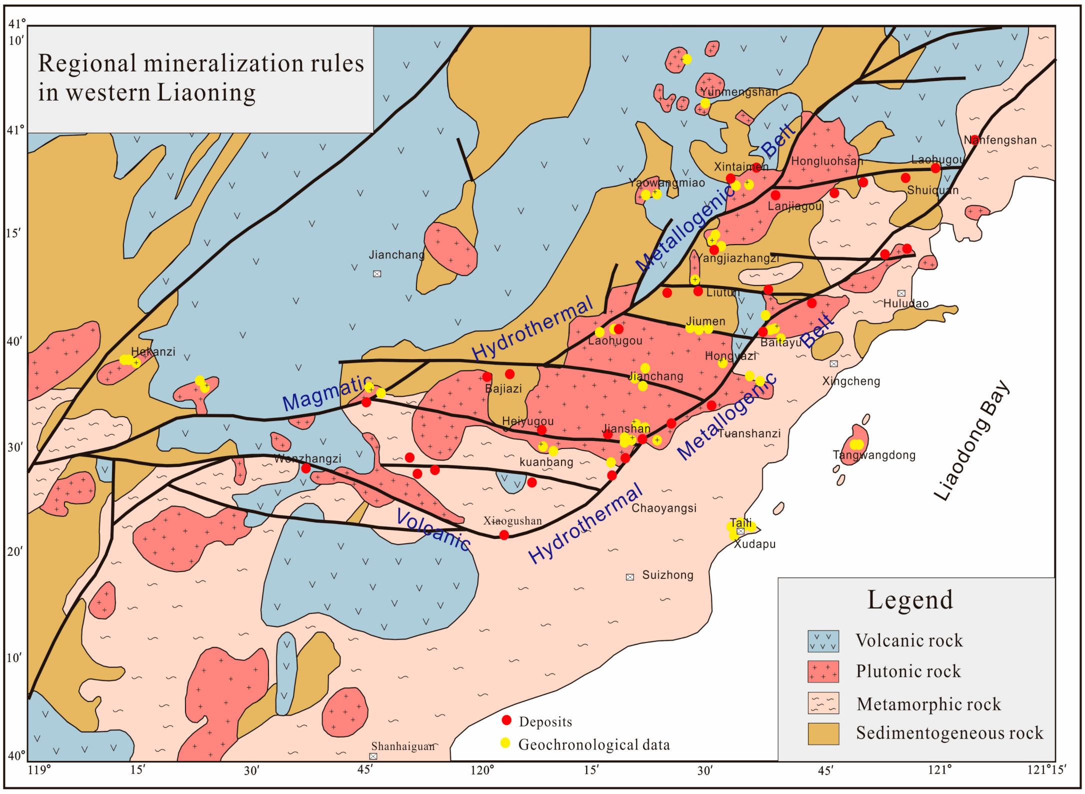

Figure 13. Regional metallogenic map of western Liaoning (Modified after [90]).

Table 3. Goechronological ages from Mesozoic deposits and magmatic rocks exposed in western Liaoning.

Area	Name of Body/Deposit	Age(Ma)	Method	Sample	Reference
Mesozoic Deposits					
Xintaimen	Molybdenum deposit	184.6 ± 1.1	Re-Os Isotope Dating	Molybdenite	Zhang et al., 2009 [74]
Xintaimen	Molybdenum deposit	182.4 ± 1.5	Re-Os Isotope Dating	Molybdenite	Zhang et al., 2009 [74]
Xintaimen	Molybdenum deposit	176.9 ± 3.7	Re-Os Isotope Dating	Molybdenite	Zhang et al., 2009 [74]
Xintaimen	Molybdenum deposit	181.6 ± 2.1	Re-Os Isotope Dating	Molybdenite	Zhang et al., 2009 [74]
Xintaimen	Molybdenum deposit	179.7 ± 3.3	Re-Os Isotope Dating	Molybdenite	Zhang et al., 2009 [74]
Huanglongpu	Caibonatite vein-type Mo(Pb) deposit	230 ± 7	Re-Os Isotope Dating	Pyrite+Molybdenite+Quartz+Galena	Huang et al., 1994 [75]
Huanglongpu	Caibonatite vein-type Mo(Pb) deposit	222 ± 8	Re-Os Isotope Dating	Pyrite+Molybdenite+Quartz+Galena	Huang et al., 1994 [75]
Huanglongpu	Caibonatite vein-type Mo(Pb) deposit	227 ± 7	Re-Os Isotope Dating	Pyrite+Molybdenite+Quartz+Galena	Huang et al., 1994 [75]
Huanglongpu	Caibonatite vein-type Mo(Pb) deposit	231 ± 7	Re-Os Isotope Dating	Pyrite+Molybdenite+Quartz+Galena	Huang et al., 1994 [75]
Huanglongpu	Caibonatite vein-type Mo(Pb) deposit	220 ± 5	Re-Os Isotope Dating	Pyrite+Molybdenite+Quartz+Galena	Huang et al., 1994 [75]
Jinduicheng	Porphy molybdenum deposit	129 ± 7	Re-Os Isotope Dating	Pyrite+Molybdenite+Quartz	Huang et al., 1994 [75]
Jinduicheng	Porphy molybdenum deposit	131 ± 4	Re-Os Isotope Dating	Pyrite+Molybdenite+Quartz+K-feldspar	Huang et al., 1994 [75]
Jinduicheng	Porphy molybdenum deposit	139 ± 3	Re-Os Isotope Dating	Molybdenite	Huang et al., 1994 [75]
Shijiawan	Porphy molybdenum deposit	138 ± 8	Re-Os Isotope Dating	Pyrite+Molybdenite+Quartz	Huang et al., 1994 [75]
Nannihu-Sandaozhuang	Porphy-skarn Mo(W) deposit	146 ± 5	Re-Os Isotope Dating	K-feldspar+Molybdenite+Quartz	Huang et al., 1994 [75]
Nannihu-Sandaozhuang	Porphy-skarn Mo(W) deposit	146 ± 6	Re-Os Isotope Dating	Molybdenite+Quartz+Zeolite	Huang et al., 1994 [75]
Nannihu-Sandaozhuang	Porphy-skarn Mo(W) deposit	156 ± 8	Re-Os Isotope Dating	Molybdenite+Quartz	Huang et al., 1994 [75]
Nannihu-Sandaozhuang	Porphy-skarn Mo(W) deposit	148 ± 10	Re-Os Isotope Dating	Molybdenite	Huang et al., 1994 [75]
Nannihu-Sandaozhuang	Porphy-skarn Mo(W) deposit	147 ± 6	Re-Os Isotope Dating	Molybdenite	Huang et al., 1994 [75]
Nannihu-Sandaozhuang	Porphy-skarn Mo(W) deposit	151 ± 4	Re-Os Isotope Dating	Molybdenite	Huang et al., 1994 [75]
Liutun, Liaoning	Gold deposit	185	K-Ar Isotope Dating	Diorite	Li and Hou, 1995 [76]
Liutun, Liaoning	Gold deposit	183	K-Ar Isotope Dating	Diorite	Li and Hou, 1995 [76]
Liutun, Liaoning	Gold deposit	160	K-Ar Isotope Dating	Diorite	Li and Hou, 1995 [76]
Liutun, Liaoning	Gold deposit	191	K-Ar Isotope Dating	Diorite	Li and Hou, 1995 [76]
Shuiquan, Liaoning	Gold deposit	239.8		Coarse-grained diorite	Dai, 2015 [77]
Shuiquan, Liaoning	Gold deposit	160		Coarse-grained diorite	Dai, 2015 [77]
Shuiquan, Liaoning	Gold deposit	150		Granite Porphyry	Dai, 2015 [77]
Shuiquan, Liaoning	Gold deposit	118.2		Granite Porphyry	Dai, 2015 [77]
Jianping, Liaoxi	Gold deposit	160.1 ± 1.1	U-Pb, LA-ICPMS	Zircon(Porphyritic biotite adamellite)	Chen et al., 2016 [78]
Jianping, Liaoxi	Gold deposit	160.2 ± 4.4	U-Pb, LA-ICPMS	Zircon(Fine-grained biotite adamellite)	Chen et al., 2016 [78]
Jianping, Liaoxi	Gold deposit	159.1 ± 1.5	U-Pb, LA-ICPMS	Zircon(Coarse-grained biotite adamellite)	Chen et al., 2016 [78]
Yuerya, Jidong	Gold deposit	171.7 ± 3.0	Re-Os Isotope Dating	Molybdenite	Chen et al., 2014 [79]
Yuerya, Jidong	Gold deposit	169.6 ± 2.4	Re-Os Isotope Dating	Molybdenite	Chen et al., 2014 [79]
Yuerya, Jidong	Gold deposit	170.8 ± 2.7	Re-Os Isotope Dating	Molybdenite	Chen et al., 2014 [79]
Yuerya, Jidong	Gold deposit	169.5 ± 2.5	Re-Os Isotope Dating	Molybdenite	Chen et al., 2014 [79]
Yuerya, Jidong	Gold deposit	168.7 ± 2.4	Re-Os Isotope Dating	Molybdenite	Chen et al., 2014 [79]
Yuerya, Jidong	Gold deposit	168.4 ± 2.5	Re-Os Isotope Dating	Molybdenite	Chen et al., 2014 [79]
Yuerya, Jidong	Gold deposit	171.1 ± 2.6	Re-Os Isotope Dating	Molybdenite	Chen et al., 2014 [79]
Xiayingfang, Jidong	Gold deposit	164.2 ± 2.3	Re-Os Isotope Dating	Molybdenite	Zou et al., 2016 [80]

Table 3. *Cont.*

Area	Name of Body/Deposit	Age(Ma)	Method	Sample	Reference
Xiaotongjiapuzi, Liaoning	Gold deposit	209 ± 16	Ar-Ar Dating	Sericite	Liu and Ai, 2002 [81]
Xiaotongjiapuzi, Liaoning	Gold deposit	169 ± 5	Ar-Ar Dating	Sericite	Liu and Ai, 2002 [81]
Xiaotongjiapuzi, Liaoning	Gold deposit	165 ± 4	Ar-Ar Dating	Sericite	Liu and Ai, 2002 [81]
Xiaotongjiapuzi, Liaoning	Gold deposit	167 ± 3	Ar-Ar Dating	Sericite	Liu and Ai, 2002 [81]
Xiaotongjiapuzi, Liaoning	Gold deposit	172 ± 6	Ar-Ar Dating	Sericite	Liu and Ai, 2002 [81]
Xiaotongjiapuzi, Liaoning	Gold deposit	197 ± 8	Ar-Ar Dating	Sericite	Liu and Ai, 2002 [81]
Xiaotongjiapuzi, Liaoning	Gold deposit	214 ± 16	Ar-Ar Dating	Sericite	Liu and Ai, 2002 [81]
Xiaotongjiapuzi, Liaoning	Gold deposit	226 ± 20	Ar-Ar Dating	Sericite	Liu and Ai, 2002 [81]
Yaojiagou	Molybdenum deposit	167.1	Re-Os Isotope Dating	Molybdenite	Fang et al., 2012 [82]
Yaojiagou	Molybdenum deposit	166.4	Re-Os Isotope Dating	Molybdenite	Fang et al., 2012 [82]
Yaojiagou	Molybdenum deposit	168.1	Re-Os Isotope Dating	Molybdenite	Fang et al., 2012 [82]
Yaojiagou	Molybdenum deposit	167.8	Re-Os Isotope Dating	Molybdenite	Fang et al., 2012 [82]
Yaojiagou	Molybdenum deposit	169.1	Re-Os Isotope Dating	Molybdenite	Fang et al., 2012 [82]
Yaojiagou	Molybdenum deposit	168.7	Re-Os Isotope Dating	Molybdenite	Fang et al., 2012 [82]
Yaojiagou	Molybdenum deposit	166.1	Re-Os Isotope Dating	Molybdenite	Fang et al., 2012 [82]
Yaojiagou	Molybdenum deposit	167.5	Re-Os Isotope Dating	Molybdenite	Fang et al., 2012 [82]
Xiaojiayingzi	Molybdenum deposit	160.8 ± 3.2	Re-Os Isotope Dating	Molybdenite	Dai et al., 2007 [83]
Xiaojiayingzi	Molybdenum deposit	161.8 ± 2.5	Re-Os Isotope Dating	Molybdenite	Dai et al., 2007 [83]
Xiaojiayingzi	Molybdenum deposit	160.6 ± 2.8	Re-Os Isotope Dating	Molybdenite	Dai et al., 2007 [83]
Xiaojiayingzi	Molybdenum deposit	159.1 ± 2.6	Re-Os Isotope Dating	Molybdenite	Dai et al., 2007 [83]
Xiaojiayingzi	Molybdenum deposit	160.4 ± 2.6	Re-Os Isotope Dating	Molybdenite	Dai et al., 2007 [83]
Xiaojiayingzi	Molybdenum deposit	165.8 ± 2.8	Re-Os Isotope Dating	Molybdenite	Dai et al., 2007 [83]
Baiyun, Liaoning	Gold deposit	757 ± 53	Ar-Ar Dating	Quartz	Liu and Ai, 2000 [84]
Baiyun, Liaoning	Gold deposit	519 ± 26	Ar-Ar Dating	Quartz	Liu and Ai, 2000 [84
Baiyun, Liaoning	Gold deposit	270 ± 15	Ar-Ar Dating	Quartz	Liu and Ai, 2000 [84]
Baiyun, Liaoning	Gold deposit	210 ± 8	Ar-Ar Dating	Quartz	Liu and Ai, 2000 [84]
Baiyun, Liaoning	Gold deposit	208 ± 6	Ar-Ar Dating	Quartz	Liu and Ai, 2000 [84]
Baiyun, Liaoning	Gold deposit	213 ± 9	Ar-Ar Dating	Quartz	Liu and Ai, 2000 [84]
Baiyun, Liaoning	Gold deposit	243 ± 12	Ar-Ar Dating	Quartz	Liu and Ai, 2000 [84]
Baiyun, Liaoning	Gold deposit	568 ± 32	Ar-Ar Dating	Quartz	Liu and Ai, 2000 [84]
Baiyun, Liaoning	Gold deposit	815 ± 65	Ar-Ar Dating	Quartz	Liu and Ai, 2000 [84]
Wulong, Liaoning	Gold deposit	123.2 ± 6.6	Ar-Ar Dating	Sericite	Liu et al., 2018 [85]
Wulong, Liaoning	Gold deposit	126.8 ± 1.3	Ar-Ar Dating	Sericite	Liu et al., 2018 [85]
Wulong, Liaoning	Gold deposit	126.3 ± 1.6	Ar-Ar Dating	Sericite	Liu et al., 2018 [85]
Wulong, Liaoning	Gold deposit	123.5 ± 1.2	Ar-Ar Dating	Sericite	Liu et al., 2018 [85]
Wulong, Liaoning	Gold deposit	122.3 ± 1.2	Ar-Ar Dating	Sericite	Liu et al., 2018 [85]
Wulong, Liaoning	Gold deposit	149.0 ± 4.9	Ar-Ar Dating	Sericite	Liu et al., 2018 [85]
Mesozoic magmatic rocks					
Kuanbang	Monzodiorite	182 ± 2	U-Pb, LA-ICPMS	Zircon	Wu et al., 2006 [17]
Jiumen	Porphyritic monzonitic granite	185 ± 2	U-Pb, LA-ICPMS	Zircon	Wu et al., 2006 [17]

Table 3. *Cont.*

Area	Name of Body/Deposit	Age(Ma)	Method	Sample	Reference
Jiumen	Fine-grained monzonitic granite	190 ± 3	U-Pb, LA-ICPMS	Zircon	Wu et al., 2006 [17]
Jianchang	Coarse-grained monzonitic granite	153 ± 1	U-Pb, LA-ICPMS	Zircon	Wu et al., 2006 [17]
Jianchang	Monzodiorite	157 ± 1	U-Pb, LA-ICPMS	Zircon	Wu et al., 2006 [17]
Yangjiazhangzi	Medium-grained monzonitic granite	188 ± 2	U-Pb, LA-ICPMS	Zircon	Wu et al., 2006 [17]
Yangjiazhangzi	Fine-grained monzonitic granite	189 ± 4	U-Pb, LA-ICPMS	Zircon	Wu et al., 2006 [17]
Yangjiazhangzi	Coarse-grained monzonitic granite	182 ± 2	U-Pb, LA-ICPMS	Zircon	Wu et al., 2006 [17]
Haitangshan	Coarse-grained monzonitic granite	176 ± 1	U-Pb, LA-ICPMS	Zircon	Wu et al., 2006 [17]
Haitangshan	Coarse-grained monzonitic granite	163 ± 1	U-Pb, LA-ICPMS	Zircon	Wu et al., 2006 [17]
Haitangshan	Coarse-grained monzonitic granite	152 ± 1	U-Pb, LA-ICPMS	Zircon	Wu et al., 2006 [17]
Jianlazi	Dimicaceous adamellite	154 ± 2	U-Pb, LA-ICPMS	Zircon	Wu et al., 2006 [17]
Jianlazi	Dimicaceous adamellite	169 ± 10	U-Pb, LA-ICPMS	Zircon	Wu et al., 2006 [17]
Shishan	Monzonitic granite	123 ± 3	U-Pb, LA-ICPMS	Zircon	Wu et al., 2006 [17]
Yiwulushan	Coarse-grained dimicaceous adamellite	163 ± 3	U-Pb, LA-ICPMS	Zircon	Wu et al., 2006 [17]
Yiwulushan	Gneissic granodiorite	153 ± 2	U-Pb, LA-ICPMS	Zircon	Wu et al., 2006 [17]
Taili area	Porphyritic granitic gneiss	218.74 ± 0.61	U-Pb, LA-ICPMS	Zircon	Liang et al., 2015 [28]
Taili area	Granitic aplite	212.1 ± 1.6	U-Pb, LA-ICPMS	Zircon	Liang et al., 2015 [28]
Taili area	Granitic aplite	219.7 ± 1.1	U-Pb, LA-ICPMS	Zircon	Liang et al., 2015 [28]
Taili area	Gneissic biotite adamellite	159.03 ± 0.82	U-Pb, LA-ICPMS	Zircon	Liang et al., 2015 [28]
Taili area	Gneissic biotite adamellite	152.4 ± 1.9	U-Pb, LA-ICPMS	Zircon	Liang et al., 2015 [28]
Taili area	Garnet-bearing granitic aplite	210.2 ± 2.7	U-Pb, LA-ICPMS	Zircon	Liang et al., 2015 [28]
Taili area	Porphyritic granitic gneiss	225.4 ± 2	U-Pb, LA-ICPMS	Zircon	Li, 2009 [43]; Li et al., 2013 [44]
Taili area	Porphyritic granitic gneiss	216.44 ± 0.5	U-Pb, LA-ICPMS	Zircon	Li, 2009 [43]; Li et al., 2013 [44]
Taili area	Porphyritic granitic gneiss	224.6 ± 2.5	U-Pb, LA-ICPMS	Zircon	Li, 2009 [43]; Li et al., 2013 [44]
Taili area	Porphyritic granitic gneiss	231.7 ± 2.0	U-Pb, LA-ICPMS	Zircon	Li, 2009 [43]; Li et al., 2013 [44]
Taili area	Gneissic biotite adamellite	153.7 ± 2	U-Pb, LA-ICPMS	Zircon	Li, 2009 [43]; Li et al., 2013 [44
Taili area	Biotite adamellite	153.7 ± 4.7	U-Pb, LA-ICPMS	Zircon	Li, 2009 [44]
Liangjia	Quartz syenite	246 ± 2	U-Pb, LA-ICPMS	Zircon	Yang et al., 2012 [86]
Jianfang	Quartz syenite	254 ± 2	U-Pb, LA-ICPMS	Zircon	Yang et al., 2012 [86]
Hekanzi	Nepheline-bearing syenite	225 ± 2	U-Pb, LA-ICPMS	Zircon	Yang et al., 2012 [86]
Hekanzi	Nepheline-bearing syenite	224 ± 2	U-Pb, LA-ICPMS	Zircon	Yang et al., 2012 [86]
Hekanzi	Pyroxene syenite	225 ± 3	U-Pb, LA-ICPMS	Zircon	Yang et al., 2012 [86]
Hekanzi	Nepheline-bearing syenite	226 ± 2	U-Pb, LA-ICPMS	Zircon	Yang et al., 2012 [86]
Hekanzi	Pyroxene syenite	226 ± 3	U-Pb, LA-ICPMS	Zircon	Yang et al., 2012 [86]
Baita	Rhyolitic breccia ignimbrite	165.6 ± 1.5	U-Pb, LA-ICPMS	Zircon	Song et al., 2018 [46]

Table 3. *Cont.*

Area	Name of Body/Deposit	Age(Ma)	Method	Sample	Reference
Baita	Rhyolite	159.6 ± 2.8	U-Pb, LA-ICPMS	Zircon	Lin, 2017 [45]
Baita	Rhyolite	157.6 ± 3.3	U-Pb, LA-ICPMS	Zircon	Lin, 2017 [45]
Baita	Rhyolite	149.0 ± 1.5	U-Pb, LA-ICPMS	Zircon	Lin, 2017 [45]
Baita	Trachyandesite	149.2 ± 1.9	U-Pb, LA-ICPMS	Zircon	Lin, 2017 [45]
Baita	Trachydacite	160.05 ± 0.67	U-Pb, LA-ICPMS	Zircon	Lin, 2017 [45]
Yaowangmiao-Mopanshan	Monzonitic granite	183 ± 2	U-Pb, LA-ICPMS	Zircon	Cui, 2015 [42]
Yaowangmiao-Mopanshan	Monzonitic granite	176 ± 1	U-Pb, LA-ICPMS	Zircon	Cui, 2015 [42]
Yaowangmiao-Mopanshan	Quartz diorite	194 ± 2	U-Pb, LA-ICPMS	Zircon	Cui, 2015 [42]
Yangjiazhangzi-Lanjiagou	Monzonitic granite	185 ± 1	U-Pb, LA-ICPMS	Zircon	Cui, 2015 [42]
Yangjiazhangzi-Lanjiagou	Monzonitic granite	177 ± 1	U-Pb, LA-ICPMS	Zircon	Cui, 2015 [42]
Yangjiazhangzi-Lanjiagou	Monzonitic granite	169 ± 2	U-Pb, LA-ICPMS	Zircon	Cui, 2015 [42]
Yangjiazhangzi-Lanjiagou	Syenogranite	174 ± 1	U-Pb, LA-ICPMS	Zircon	Cui, 2015 [42]
Jianchang	Monzonitic granite	161 ± 2	U-Pb, LA-ICPMS	Zircon	Cui, 2015 [42]
Yingchangkou	Monzonitic granite	156 ± 1	U-Pb, LA-ICPMS	Zircon	Cui, 2015 [42]
Yingchangkou	Monzonitic granite	157 ± 2	U-Pb, LA-ICPMS	Zircon	Cui, 2015 [42]
Moshigou	Granite porphyry	155 ± 2	U-Pb, LA-ICPMS	Zircon	Cui, 2015 [42]
Hongyazi	Monzonitic granite	139 ± 1	U-Pb, LA-ICPMS	Zircon	Cui, 2015 [42]
Tangwangdong	Quartz monzodiorite	121 ± 1	U-Pb, LA-ICPMS	Zircon	Cui, 2015 [42]
Tangwangdong	Quartz syenite	125 ± 1	U-Pb, LA-ICPMS	Zircon	Cui, 2015 [42]
Yiwulushan	Granite	162.8 ± 3.9	U-Pb, SHRIMP	Zircon	Cui, 2015 [42]
Yiwulushan	Granite	159.1 ± 3.6	U-Pb, SHRIMP	Zircon	Cui, 2015 [42]
Dashipo	Granite	196.5 ± 1.9	U-Pb, SHRIMP	Zircon	Deng et al., 2004 [87]
Sigangding	Quartz monzonite	159.3 ± 1.9	U-Pb, SHRIMP	Zircon	Deng et al., 2004 [87]
Shicheng	Gneiss diorite	155.8 ± 1.5	U-Pb, SHRIMP	Zircon	Deng et al., 2004 [87]
Changyuan	Gneiss diorite	152.7 ± 3.2	U-Pb, SHRIMP	Zircon	Deng et al., 2004 [87]
Yunmengshan	Gneiss granite	144.7 ± 2.7	U-Pb, SHRIMP	Zircon	Deng et al., 2004 [87]
Guijiuyu	Granite	137.7 ± 3.6	U-Pb, SHRIMP	Zircon	Deng et al., 2004 [87]
Hanjiachuan	Quartz monzonite	137.6 ± 1.2	U-Pb, SHRIMP	Zircon	Deng et al., 2004 [87]
Qipanyan	Gabbro	132.9 ± 0.66	U-Pb, SHRIMP	Zircon	Deng et al., 2004 [87]
Bijingsi	Shaoshaolite	132	U-Pb, SHRIMP	Zircon	Deng et al., 2004 [87]
Xuejiashiliang	Granite	130 ± 1.7	U-Pb, SHRIMP	Zircon	Deng et al., 2004 [87]
Shangzhuang	Gabbro	128.8 ± 1.7	U-Pb, SHRIMP	Zircon	Deng et al., 2004 [87]
Baicha	Alkaline feldspar granite	127.03 ± 0.69	U-Pb, SHRIMP	Zircon	Deng et al., 2004 [87]
Heishanzhai	Monzonite	125.1 ± 1.5	U-Pb, SHRIMP	Zircon	Deng et al., 2004 [87]
Humeng	Syenite	124.2 ± 1.8	U-Pb, SHRIMP	Zircon	Deng et al., 2004 [87]
Heixiongshan	Granite	123.7 ± 1.1	U-Pb, SHRIMP	Zircon	Deng et al., 2004 [87]
Yanshan Belt	Trachite	184	U-Pb, SHRIMP	Zircon	Deng et al., 2006 [88]
Yanshan Belt	Trachyandesite	161	U-Pb, SHRIMP	Zircon	Deng et al., 2006 [88]

Table 3. *Cont.*

Area	Name of Body/Deposit	Age(Ma)	Method	Sample	Reference
Yanshan Belt	Trachite	167	U-Pb, SHRIMP	Zircon	Deng et al., 2006 [88]
Yanshan Belt	Trachyandesite	137	U-Pb, SHRIMP	Zircon	Deng et al., 2006 [88]
Yanshan Belt	Monzonite	197	U-Pb, SHRIMP	Zircon	Deng et al., 2006 [88]
Yanshan Belt	Quartz monzonite	159	U-Pb, SHRIMP	Zircon	Deng et al., 2006 [88]
Yanshan Belt	Quartz monzonite	153	U-Pb, SHRIMP	Zircon	Deng et al., 2006 [88]
Yanshan Belt	Quartz monzonite	138	U-Pb, SHRIMP	Zircon	Deng et al., 2006 [88]
Yanshan Belt	Quartz monzonite	136	U-Pb, SHRIMP	Zircon	Deng et al., 2006 [88]
Shicheng	Gneiss diorite	159 ± 2	U-Pb	Single zircon	Davis et al., 2001 [89]
Changyuan	Gneiss diorite	151 ± 2	U-Pb	Single zircon	Davis et al., 2001 [89]
Shatuozi	Gneiss diorite	151 ± 2	U-Pb	Single zircon	Davis et al., 2001 [89]
Jiangchang	Andesite	173 ± 6	Ar-Ar Dating		Davis et al., 2001 [89]
Shisanling	Hornblende andesite	161.1 ± 1.9	Ar-Ar Dating		Davis et al., 2001 [89]
Zhangliadian	Biotite stuff	160.7 ± 0.8	Ar-Ar Dating		Davis et al., 2001 [89]
Huangtuliang	Hornblende andesite	147.6 ± 1.6	Ar-Ar Dating		Davis et al., 2001 [89]
Lubeixiang	Volcanic rock	167.2 ± 9.7	Ar-Ar Dating		Deng et al., 2004 [87]
Chaoyang	Volcanic rock	166.5 ± 0.8	Ar-Ar Dating		Deng et al., 2004 [87]
Kasheng	Volcanic rock	165.6 ± 3.8	Ar-Ar Dating		Deng et al., 2004 [87]
Xudapu	Garnet-bearing adamellite	152 ± 4	U-Pb, LA-ICPMS		This study
Xudapu	Garnet-bearing adamellite	158 ± 3	U-Pb, LA-ICPMS		This study
Xudapu	Biotie adamellite	168 ± 2	U-Pb, LA-ICPMS		This study
Xudapu	Biotie adamellite	172 ± 2	U-Pb, LA-ICPMS		This study

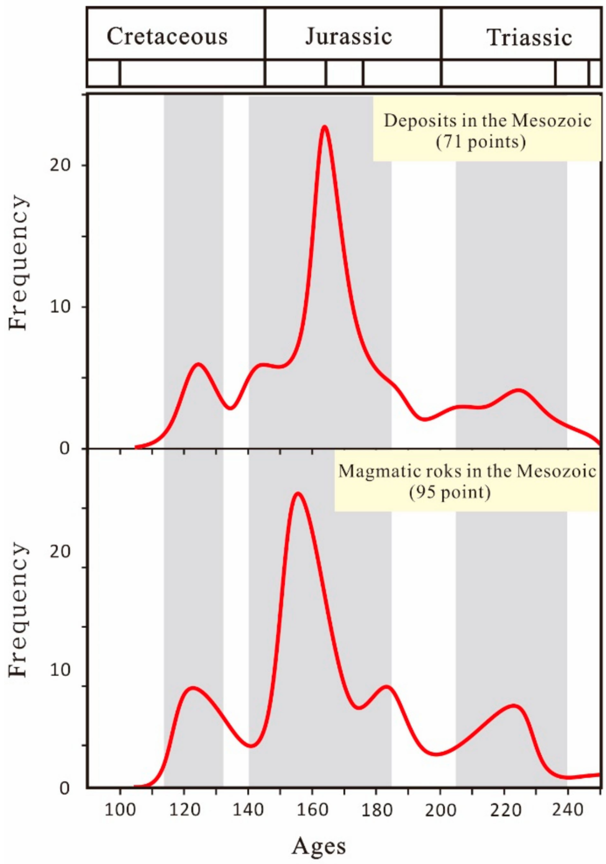

Figure 14. Frequency diagrams of compiled geochronological ages from Mesozoic deposits and magmatic rocks exposed in western Liaoning. Data sources are as follows [17,28,44,46,74–89].

7. Conclusions

Our new data allow us to deduce the following major conclusions:

(1) The Xingcheng-Xudapu area is composed dominantly of two types of granitic rocks, the biotite adamellites with emplacement ages of 172–168 Ma and the garnet-bearing adamellites with a 158–152 Ma age.

(2) The biotite adamellites are typical I-type granites formed from partial melting of the ancient crust in the setting of the subduction of the Paleo-Pacific plate beneath the north margin of the NCC. The garnet-bearing adamellites are I-type granites with characteristics both of compressional and extensional tectonic setting, which were formed in the middle-late stages of the continuing subduction of the Paleo-Pacific plate, while simultaneously the frontal side of the subduction slab began to roll back, leading to an extensional environment.

(3) The eastern segment of the northern margin of NCC had been under the control of the Paleo-Pacific tectonic domain at the latest in the Middle Jurassic (172–168 Ma), while the initiation tectonic transformation from a compressional to an extensional environment was during the Late Jurassic (158–152 Ma), as a response to the Yanshan Movement.

(4) The Mesozoic endogenetic metalliferous deposits in western Liaoning formed in a compressive environment influenced by the subduction of the Paleo-Pacific plate similar to the magma events in the North of NCC, and the magmatism provided the thermodynamic condition and the source of metallogenic hydrothermal fluid for mineralization.

Author Contributions: P.H. and C.L. conceived of the presented idea, designed the experiments and verified the data toghther. The article is originally written and revised by the corresponding author, C.L., the other authors are also responsible for many revisions. The financial support for this study was mainly secured by C.L. and C.Z.,

X.Z., Y.Y. and E.Z. digitalized the geological map and performed LA-ICP-MS dating and geochemistry analysis along with P.H.

Funding: This project was financially co-supported by the National Key R&D Program of China (Grant No. 2017YFC0601401) and National Natural Science Foundation of China (Grant no. 41602211, 41872192 and 41772164).

Acknowledgments: We acknowledge detailed comments of three anonymous reviewers who helped clarify ideas and presentations. The authors also acknowledge polishing of the English by Qi Zheng from School of Foreign Language Education, Jilin University.

Conflicts of Interest: The authors declare no conflict of interest.

References

1. Wong, B.W.H. Crustal movements and igneous activities in eastern China since Mesozoic time. *Bull. Geol. Soc. China* **1927**, *6*, 9–37. [CrossRef]
2. Guo, P.; Niu, Y.; Ye, L.; Liu, J.; Sun, P.; Cui, H.; Zhang, Y.; Gao, J.; Su, L.; Zhao, J.; et al. Lithosphere thinning beneath west North China Craton: Evidence from geochemical and Sr-Nd-Hf isotope compositions of Jining basalts. *Lithos* **2014**, *202*, 37–54. [CrossRef]
3. Gao, H.L.; Zhao, Y.; Ye, H.; Zhang, S.-H.; Liu, J.; Wang, G.C. Dating Jurassic volcanic rocks in the Western Hills of Beijing, North China: Implications for the initiation of the Yanshanian tectonism and subsequent thermal events. *J. Asian Earth Sci.* **2018**, *161*, 164–177. [CrossRef]
4. Li, S.; Zhao, G.; Dai, L.; Liu, X.; Zhou, L.; Santosh, M.; Suo, Y. Mesozoic basins in eastern China and their bearing on the deconstruction of the North China Craton. *J. Asian Earth Sci.* **2012**, *47*, 64–79. [CrossRef]
5. Yang, F.Q.; Wu, H.; Pirajno, F.; Ma, B.Y.; Xia, H.D.; Deng, H.J.; Liu, X.W.; Xu, G.; Zhao, Y. The jiashan syenite in northern hebei: An early record of lithospheric thinning in the yanshan intracontinental orogenic belt. *Geol. Rev.* **2007**, *29*, 619–636. [CrossRef]
6. Dai, L.; Li, S.; Li, Z.-H.; Somerville, I.; Suo, Y.; Liu, X.; Gerya, T.; Santosh, M. Dynamics of exhumation and deformation of HP-UHP orogens in double subduction-collision systems: Numerical modeling and implications for the Western Dabie Orogen. *Earth Sci. Rev.* **2018**, *182*, 68–84. [CrossRef]
7. Li, Z.-H.; Dong, S.-W.; Qu, H.-J. Timing of the initiation of the Jurassic Yanshan movement on the North China Craton: Evidence from sedimentary cycles, heavy minerals, geochemistry, and zircon U–Pb geochronology. *Int. Geol. Rev.* **2013**, *56*, 288–312. [CrossRef]
8. Dong, S.; Zhang, Y.; Li, H.; Shi, W.; Xue, H.; Li, J.; Huang, S.; Wang, Y. The Yanshan orogeny and late Mesozoic multi-plate convergence in East Asia—Commemorating 90th years of the "Yanshan Orogeny". *Sci. China Earth Sci.* **2018**, *61*, 1888–1909. [CrossRef]
9. Zheng, Y.D.; Davis, G.A.; Wang, C.; Darby, B.J.; Zhang, C.H. Major Mesozoic Tectonic Events in the Yanshan Belt and the Plate Tectonic Setting. *Acta Geol. Sinica.* **2000**, *74*, 289–302, (In Chinese with English Abstract).
10. Maruyama, S. Pacific-type Orogeny Revisited: Miyashiro-Type Orogeny Proposed. *Isl. Arc.* **1997**, *6*, 91–120. [CrossRef]
11. Zhao, Y.; Xu, G.; Zhang, S.H.; Yang, Z.Y.; Zhang, Y.Q.; Hu, J.M. Yanshanian movement and conversion of tectonic regimes in East Asia. *Earth Sci. Front.* **2004**, *11*, 319–328, (In Chinese with English Abstract).
12. Kojima, S.; Kemkin, I.; Kametaka, M.; Ando, A. A Correlation of-Accretionary Complexs of Southern Sikhote-Alin of Russia and Zone of Southwest Japan. *Geosci. J.* **2000**, *4*, 175–185. [CrossRef]
13. Wang, Y.; Dong, S.; Chen, X.; Shi, W. New time constraint on the initiation of Yanshan movement from Jurassic growth strata in the Daqingshan area, Inner Mongolia. *Chin. Sci. Bull.* **2017**, *62*, 1274–1277. [CrossRef]
14. Zhai, M.; Santosh, M. Metallogeny of the North China Craton: Link with secular changes in the evolving Earth. *Gondwana Res.* **2013**, *24*, 275–297. [CrossRef]
15. Dong, S.W.; Zhang, Y.Q.; You, C.X.; Yang, Z.Y.; Ji, Q.; Wang, T.; Hu, J.M.; Chen, X.H. Jurassic Tectonic Revolution in China and New Interpretation of the Yanshan Movement. *Acta Geol. Sin.* **2007**, *81*, 1449–1461, (In Chinese with English Abstract).
16. Ren, J.S. The Indosinian orogeny and its significance in the tectonic evolution of China. *Bull. Chin. Acad. Geolog. Sci.* **1984**, *9*, 31–44, (In Chinese with English Abstract).
17. Wu, F.Y.; Yang, J.H.; Zhang, Y.B.; Liu, X.M. Emplacement ages of the Mesozoic granites in southeastern part of the Western Liaoning Province. *Acta Petrol. Sinica.* **2006**, *22*, 315–325, (In Chinese with English Abstract).

18. Qiu, R.; Zhou, S.; Tan, Y.; Liu, Z.; Xiao, Q.; Feng, Y.; Zhang, G. Deep-Setting of the Large-scale Magmatism and Mineralization in Late Mesozoic of the Eastern China. *Acta Geol. Sin.* **2014**, *88*, 33–34. [CrossRef]
19. Chen, Y.; Guo, G.; Li, X. Metallogenic geodynamic background of Mesozoic gold deposits in granite-greenstone terrains of North China Craton. *Sci. China Ser. D Earth Sci.* **1998**, *41*, 113–120. [CrossRef]
20. Mao, J.W. Geodynamic settings of Mesozoic large-scale mineralization in North China and adjacent areas. *Sci. China (Ser. D)* **2003**, *46*, 838–851. [CrossRef]
21. Li, J.-W.; Bi, S.-J.; Selby, D.; Chen, L.; Vasconcelos, P.; Thiede, D.; Zhou, M.-F.; Zhao, X.-F.; Li, Z.-K.; Qiu, H.-N. Giant Mesozoic gold provinces related to the destruction of the North China craton. *Earth Planet. Sci. Lett.* **2012**, *349*, 26–37. [CrossRef]
22. Mao, J.-W.; Xie, G.-Q.; Pirajno, F.; Ye, H.-S.; Wang, Y.-B.; Li, Y.-F.; Xiang, J.-F.; Zhao, H.-J. Late Jurassic–Early Cretaceous granitoid magmatism in Eastern Qinling, central-eastern China: SHRIMP zircon U–Pb ages and tectonic implications. *Aust. J. Earth Sci.* **2010**, *57*, 51–78. [CrossRef]
23. Wei, P.F.; Yu, X.F.; Li, D.P.; Liu, Q.; Yu, L.D.; Li, Z.S.; Geng, K.; Zhang, Y.; Sun, Y.Q.; Chi, N.J. Geochemistry, Zircon U–Pb Geochronology, and Lu-Hf Isotopes of the Chishan Alkaline Complex, Western Shandong, China. *Minerals* **2019**, *9*, 293. [CrossRef]
24. Yang, J.H.; Zhou, X.H. Rb-Sr, Sm-Nd, and Pb isotope systematics of pyrite: Implications for the age and genesis of lode gold deposits. *Geology* **2001**, *29*, 711–714. [CrossRef]
25. Wu, F.-Y.; Lin, J.-Q.; Wilde, S.A.; Zhang, X.; Yang, J.-H. Nature and significance of the Early Cretaceous giant igneous event in eastern China. *Earth Planet. Sci. Lett.* **2005**, *233*, 103–119. [CrossRef]
26. Lopes, A.A.C.; Moura, M.A. The Tocantinzinho Paleoproterozoic Porphyry-Style Gold Deposit, Tapajós Mineral Province (Brazil): Geology, Petrology and Fluid Inclusion Evidence for Ore-Forming Processes. *Minerals* **2019**, *9*, 29. [CrossRef]
27. Zaitsev, A.I.; Fridovsky, V.Y.; Kudrin, M.V. Granitoids of the ergelyakh intrusion-related gold-bismuth deposit (Kular-Nera Slate Belt, Northeast Russia): Petrology, physicochemical parameters of formation, and ore potential. *Minerals* **2019**, *9*, 297. [CrossRef]
28. Liang, C.; Liu, Y.; Neubauer, F.; Jin, W.; Zeng, Z.; Genser, J.; Li, W.; Li, W.; Han, G.; Wen, Q.; et al. Structural characteristics and LA–ICP-MS U–Pb zircon geochronology of the deformed granitic rocks from the Mesozoic Xingcheng-Taili ductile shear zone in the North China Craton. *Tectonophys* **2015**, *650*, 80–103. [CrossRef]
29. Liu, D.Y.; Nutman, A.P.; Compston, W.; Wu, J.S.; Shen, Q.H. Remnants of ≥3800 Ma crust in the Chinese part of the Sino-Korean craton. *Geology* **1992**, *20*, 339–342. [CrossRef]
30. Gao, S.; Zhang, J.; Xu, W.; Liu, Y. Delamination and destruction of the North China Craton. *Sci. Bull.* **2009**, *54*, 3367–3378. [CrossRef]
31. Menzies, M.A.; Fan, W.; Zhang, M. Palaeozoic and Cenozoic lithoprobes and the loss of >120 km of Archaean lithosphere, Sino-Korean craton, China. *Geol. Soc. Lond. Spéc. Publ.* **1993**, *76*, 71–81. [CrossRef]
32. Yu, S.; Li, S.; Zhang, J.; Peng, Y.; Somerville, I.; Liu, Y.; Wang, Z.; Li, Z.; Yao, Y.; Li, Y. Multistage anatexis during tectonic evolution from oceanic subduction to continental collision: A review of the North Qaidam UHP Belt, NW China. *Earth Sci. Rev.* **2019**, *191*, 190–211. [CrossRef]
33. Zhu, R.X.; Fan, H.R.; Li, J.W.; Meng, Q.R.; Li, S.R.; Zeng, Q.D. Decratonic gold deposits. *Sci. China Earth Sci.* **2015**, *58*, 1523–1537. [CrossRef]
34. Zhu, R.; Chen, L.; Wu, F.; Liu, J. Timing, scale and mechanism of the destruction of the North China Craton. *Sci. China Earth Sci.* **2011**, *54*, 789–797. [CrossRef]
35. Wu, F.Y.; Xu, Y.G.; Zhu, R.X.; Zhang, G.W. Thinning and destruction of the cratonic lithosphere: A global perspective. *Sci. China Earth Sci.* **2014**, *57*, 2878–2890. [CrossRef]
36. Wong, B.W.H. The Mesozoic Orogenic Movement in Eastern China. *Bull. Chin. Acad. Geol. Sci.* **1929**, *8*, 33–44. [CrossRef]
37. Zhai, M.G. State of lithosphere beneath the North China Craton before the Mesozoic lithospheric disruption: A suggestion. *Geotecton. Metallog.* **2008**, *32*, 516–520.
38. Zhang, Y.; Yang, J.-H.; Sun, J.-F.; Zhang, J.-H.; Chen, J.-Y.; Li, X.-H. Petrogenesis of Jurassic fractionated I-type granites in Southeast China: Constraints from whole-rock geochemical and zircon U–Pb and Hf–O isotopes. *J. Asian Earth Sci.* **2015**, *111*, 268–283. [CrossRef]
39. Zhang, X.Z.; Yang, B.J.; Wu, F.Y.; Liu, G.X. The lithosphere structure of Northeast China. *Front. Earth Sci.* **2007**, *1*, 165–171. [CrossRef]

40. Wang, G.H.; Zhang, C.H.; Wang, G.S.; Wu, Z.W. Tectonic framework of western Liaoning province and its evolution during Mesozoic. *Geoscience* **2001**, *15*, 1–7, (In Chinese with English Abstract).
41. Xu, C.G.; Xu, X.S.; Qiu, D.Z. Structural and sequence stratigraphic frameworks and palaeogeography of the Paleogene in central-southern Liaoxi Sag, Liaodongwan Bay area. *J. Palaeogeogr.* **2005**, *7*, 449–459.
42. Cui, F.H. Petrogenesis of Mesozoic Granitoids and Crustal Evolution in Xingcheng Area, Western Liaoning Province. Ph.D. Thesis, Jilin University, Changchun, China, 2015; pp. 32–107.
43. Li, J. Charateristics of Granitic Rocks and Its Geological Significance in Taili Area of Western Liaoning Province. Ph.D. Thesis, Jilin University, Changchun, China, 2009; pp. 32–41.
44. Li, J.; Zhang, X.; Jin, W.; Zheng, P.X. Characteristics of Porphyritic Granitic Gneiss in Taili Area, Western Liaoning Province and Their Geological Significance. *Geol. J. China Univ.* **2013**, *19*, 259–273, (In Chinese with English Abstract).
45. Song, Y.; Xu, X.C.; Zheng, C.Q.; Lin, B.; Meng, Z.H.; Xu, J.L. Petrology, isotopic geochronology and geochemistry of Jurassic volcanic rocks in Baita area, western Liaoning. *Glob. Geol.* **2018**, *37*, 70–87.
46. Lin, B. Geochemistry and Petrogenesis of Mesozoic Volcanic Rocks in the Geological Corridor of Western Liaoning. Ph.D. Thesis, Jilin University, Changchun, China, 2017; pp. 85–121.
47. Wang, T.; Guo, L.; Zheng, Y.; Donskaya, T.; Gladkochub, D.; Zeng, L.; Li, J.; Wang, Y.; Mazukabzov, A. Timing and processes of late Mesozoic mid-lower-crustal extension in continental NE Asia and implications for the tectonic setting of the destruction of the North China Craton: Mainly constrained by zircon U-Pb ages from metamorphic core complexes. *Lithos* **2012**, *154*, 315–345. [CrossRef]
48. Dai, J.Z.; Mao, J.W.; Zhao, C.S.; Li, F.R.; Wang, R.T.; Xie, G.Q.; Yang, F.Q. Zircon SHRIMP U-Pb Age and Petrogeochemical Features of the Lanjiagou Granite in Western Liaoning Province. *Acta Geol. Sin.* **2008**, *82*, 1555–1564, (In Chinese with English Abstract).
49. Chen, S.B.; Zhang, Y.; Guo, P.J.; Zhao, Y.; Xie, M.H. Rock spectral measurements and their characterization analysis in Xingcheng Area, Liaoning Province. *J. Jilin Univ. (Earth Sci. Ed.)* **2015**, *45*, 320–326.
50. Liu, Y.; Hu, Z.; Gao, S.; Günther, D.; Xu, J.; Gao, C.; Chen, H. In situ analysis of major and trace elements of anhydrous minerals by LA-ICP-MS without applying an internal standard. *Chem. Geol.* **2008**, *257*, 34–43. [CrossRef]
51. Ludwing, K.R. ISOPLOT 3: A geochronological tookit for Microsoft Excel. *Geochronol. Centre* **2003**, *4*, 1–72.
52. Irvine, T.N.; Baragar, W.R.A. A Guide to the Chemical Classification of the Common Volcanic Rocks. *Can. J. Earth Sci.* **1970**, *8*, 523–548. [CrossRef]
53. Peccerillo, A.; Taylor, S.R. Geochemistry of eocene calc-alkaline volcanic rocks from the Kastamonu area, Northern Turkey. *Contrib. Miner. Pet.* **1976**, *58*, 63–81. [CrossRef]
54. Middlemost, E.A. Naming materials in the magma/igneous rock system. *Earth Sci. Rev.* **1994**, *37*, 215–224. [CrossRef]
55. Sun, S.-S.; Mc Donough, W. Chemical and isotopic systematics of oceanic basalts: Implications for mantle composition and processes. *Geol. Soc. Lond. Spé301;c. Publ.* **1989**, *42*, 313–345. [CrossRef]
56. Jahn, B.-M.; Wu, F.; Capdevila, R.; Martineau, F.; Zhao, Z.; Wang, Y. Highly evolved juvenile granites with tetrad REE patterns: The Woduhe and Baerzhe granites from the Great Xing'an Mountains in NE China. *Lithos* **2001**, *59*, 171–198. [CrossRef]
57. Wu, F.-Y.; Sun, D.-Y.; Jahn, B.-M.; Wilde, S. A Jurassic garnet-bearing granitic pluton from NE China showing tetrad REE patterns. *J. Asian Earth Sci.* **2004**, *23*, 731–744. [CrossRef]
58. Wu, F.Y.; Li, X.H.; Yang, J.H.; Zheng, Y.F. Dicussions on the petrogenesis of granites. *Acta Geol. Sin.* **2007**, *23*, 1217–1238.
59. Collins, W.J.; Beams, S.D.; White, A.J.; Verhoogen, J. Nature and origin of A-type granites with particularrefrence to south-eastern Australia, Contrib. *Contrib. Mineral. Petrol.* **1982**, *80*, 189–200. [CrossRef]
60. Whalen, J.B.; Currie, K.L.; Chapell, B.W. A-type granites: Geochemical characteristics, discriminatuon and petrogenesis. *Contrib. Mineral. Petrol.* **1987**, *95*, 142–150. [CrossRef]
61. Pearce, J.A.; Harris, N.B.W.; Tindle, A.G. Trace Element Discrimination Diagrams for the Tectonic Interpretation of Granitic Rocks. *J. Pet.* **1984**, *25*, 956–983. [CrossRef]
62. Li, S.; Suo, Y.; Li, X.; Zhou, J.; Santosh, M.; Wang, P.; Wang, G.; Guo, L.; Yu, S.; Lan, H.; et al. Mesozoic tectono-magmatic response in the East Asian ocean-continent connection zone to subduction of the Paleo-Pacific Plate. *Earth Sci. Rev.* **2019**, *192*, 91–137. [CrossRef]

63. Zhu, R.; Zhang, H.; Zhu, G.; Meng, Q.; Fan, H.; Yang, J.; Wu, F.; Zhang, Z.; Zheng, T. Craton destruction and related resources. *Acta Diabetol.* **2017**, *106*, 2233–2257. [CrossRef]
64. Fan, W.; Martin, M. Destruction of aged lower lithosphere and accretion of asthenosphere mantle beneath eastern China. *Geotecton. Metall.* **1992**, *16*, 171–180.
65. Yu, S.Y.; Zhang, J.X.; Li, S.Z.; Santosh, M.; Li, Y.S.; Liu, Y.J.; Li, X.Y.; Peng, Y.B.; Sun, D.Y.; Wang, Z.Y.; et al. TTG-Adakitic-Like (Tonalitic-Trondhjemitic) Magmas Resulting From Partial Melting of Metagabbro Under High-Pressure Condition During Continental Collision in the North Qaidam UHP Terrane, Western China. *Tectonics* **2019**, *38*, 791–822. [CrossRef]
66. Gao, S.; Rudnick, R.L.; Yuan, H.-L.; Liu, X.-M.; Liu, Y.-S.; Xu, W.-L.; Ling, W.-L.; Ayers, J.; Wang, X.-C.; Wang, Q.-H. Recycling lower continental crust in the North China craton. *Nature* **2004**, *432*, 892–897. [CrossRef] [PubMed]
67. Davis, G.A.; Darby, B.J.; Yadong, Z.; Spell, T.L. Geometric and temporal evolution of an extensional detachment fault, Hohhot metamorphic core complex, Inner Mongolia, China. *Geology* **2002**, *30*, 1003–1006. [CrossRef]
68. Liu, J.; Davis, G.A.; Lin, Z.; Wu, F. The Liaonan metamorphic core complex, Southeastern Liaoning Province, North China: A likely contributor to Cretaceous rotation of Eastern Liaoning, Korea and contiguous areas. *Tectonophys* **2005**, *407*, 65–80. [CrossRef]
69. Kröner, A.; Cui, W.; Wang, S.; Wang, C.; Nemchin, A.; Nemchin, A. Single zircon ages from high-grade rocks of the Jianping Complex, Liaoning Province, NE China. *J. Asian Earth Sci.* **1998**, *16*, 519–532. [CrossRef]
70. Dhuime, B.; Cawood, P.; Hawkesworth, C. Detrital zircon record and tectonic setting. *Geology* **2012**, *40*, 875–878.
71. Liu, W.; Liu, X.; Pan, J.; Wang, K.; Wang, G.; Niu, Y.; Gong, W. Magma Mixing Genesis of the Mafic Enclaves in the Qingshanbao Complex of Longshou Mountain, China: Evidence from Petrology, Geochemistry, and Zircon Chronology. *Minerals* **2019**, *9*, 195. [CrossRef]
72. Yang, J.; Zhao, L.; Kaus, B.J.; Lu, G.; Wang, K.; Zhu, R. Slab-triggered wet upwellings produce large volumes of melt: Insights into the destruction of the North China Craton. *Tectonophys* **2018**, *746*, 266–279. [CrossRef]
73. Xu, W.L.; Wang, Q.H.; Wang, D.Y.; Pei, F.P.; Gao, S. Processes and mechanism of Mesozoic lithospheric thinning in eastern North China Craton: Evidence from Mesozoic igneous rocks and deep-seated xenoliths. *Earth Sci. Front.* **2004**, *11*, 309–317, (In Chinese with English Abstract).
74. Zhang, Z.Z.; Wu, C.Z.; Gu, L.X.; Feng, H.; Zheng, Y.C.; Huang, J.H.; Li, J.; Sun, Y.L. Molybdenite Re-Os dating of Xintaimen molybdenum deposit in Yanshan-Liaoning metallogenic belt, North China. *Miner. Depos.* **2009**, *28*, 313–320, (In Chinese with English Abstract).
75. Huang, D.H.; Wu, C.Y.; Du, A.D.; He, H.L. Re-Os Isotope Ages of Molybdenum Deposits in East Qinling and Their Significance. *Miner. Depos.* **1994**, *13*, 221–230, (In Chinese with English Abstract). [CrossRef]
76. Li, G.K.; Hou, Z.Y. The Geological Characteristics of Liutun Gold Deposit and its Genesis. *J. Precious Met. Geol.* **1995**, *4*, 67–74, (In Chinese with English Abstract).
77. Dai, L.D. Geological characteristics and potentials of deep ore prospecting in Shuiquan Gold Deposit in Liaoning. *Gold* **2015**, *36*, 27–30, (In Chinese with English Abstract).
78. Chen, J.S.; Peng, Y.D.; Liu, M.; Xing, D.H.; Li, W.W. Zircon U-Pb geochronology, geochemical characteristics and geological significance of the pluton in the Shaoguoyingzi gold ore deposit in Jianping, western Liaoning. *Geol. China* **2016**, *43*, 395–409, (In Chinese with English Abstract).
79. Chen, S.C.; Ye, H.S.; Wang, Y.T.; Zhang, X.K.; Lu, D.Y.; Hu, H.B. Re-Os age of molybdenite from the Yuerya Au deposit in eastern Hebei Province and its geological significance. *Geol. China* **2014**, *41*, 1565–1576, (In Chinese with English Abstract).
80. Zou, T.; Wang, Y.W.; Wang, J.B.; Zhang, H.Q.; Zhao, L.T.; Xie, H.J.; Shi, Y.; Liu, Y.Z.; Liu, G.Q. Geochronology of the Xiayingfang Au deposit eastern Hebei province. *Geol. Explor.* **2016**, *52*, 0084–0097.
81. Liu, G.P.; Ai, Y.F. Study on Ore_forming Epoch of Xiaotongjapuzi Gold Deposit, Liaoning Province. *Miner. Depos.* **2002**, *21*, 53–57.
82. Fang, J.Q.; Nie, S.J.; Zhang, K.; Liu, Y.; Xu, B. Re-Os isotopic dating on molybdenite separates and its geological significance from the Yaojiagou molybdenum deposit, Liaoning Province. *Acta Petrol. Sin.* **2012**, *28*, 372–378.

83. Dai, J.Z.; Mao, J.W.; Du, A.D.; Xie, G.Q.; Bai, J.; Yang, F.Q.; Qu, W.J. Re-Os Dating of Molybdenite from the Xiaoj iayingzi Mo(Fe)Deposit in Western Liaoning and Its Geological Significance. *Acta Geol. Sin.* **2007**, *81*, 917–923.
84. Liu, G.P.; Ai, Y.F. Studies on the mineralization age of Baiyun gold deposit in Liaoning. *Acta Petrol. Sin.* **2000**, *16*, 627–632.
85. Liu, J.; Wang, S.L.; Li, T.G.; Yang, Y.; Liu, F.X.; Li, X.H.; Duan, C. Geochronology and isotopic geochemical characteristics of Wulong gold deposit in Liaoning Province. *Miner. Depos.* **2018**, *37*, 712–728.
86. Yang, J.-H.; Sun, J.-F.; Zhang, M.; Wu, F.-Y.; Wilde, S.A. Petrogenesis of silica-saturated and silica-undersaturated syenites in the northern North China Craton related to post-collisional and intraplate extension. *Chem. Geol.* **2012**, *328*, 149–167. [CrossRef]
87. Deng, J.F.; Su, S.G.; Mo, X.X.; Zhao, G.C.; Xiao, Q.H.; Ji, G.Y.; Qiu, R.Z.; Zhao, H.L.; Luo, Z.H.; Wang, Y.; et al. The Sequence of Magmatic-Tectonic Events and Orogenic Processes of the Yanshan Belt, North China. *Acta Geol. Sin.* **2004**, *78*, 260–266.
88. Deng, J.F.; Su, S.G.; Liu, C.L.; Zhao, G.C.; Zhao, X.G.; Zou, S.; Wu, Z.X. Discussion on the lithospheric thinning of the North China craton: Delamination? Or thermal erosion and chemical metasomatism? *Earth Sci. Front.* **2006**, *13*, 105–119, (In Chinese with English Abstract).
89. Davis, G.A.; Yadong, Z.; Cong, W.; Darby, B.J.; Changhou, Z.; Gehrels, G. Mesozoic tectonic evolution of the Yanshan fold and thrust belt, with emphasis on Hebei and Liaoning provinces, northern China. Paleozoic and Mesozoic Tectonic Evolution of Central and Eastern Asia: From Continental Assembly to Intracontinental Deformation. *Geol. Society of America.* **2001**, *194*, 171–197.
90. Ma, Y.G. Analysis if Surface Defect in Turbine Blade of DZ123 Superalloy. *Non Ferr. Min. Metall.* **2019**, *35*, 7–9.
91. Mao, J.W.; Pirajno, F.; Xiang, J.F.; Gao, J.J.; Ye, H.S.; Li, Y.F.; Guo, B.J. Mesozoic molybdenum deposits in the east Qinling-Dabie oro-genic belt: Characteristics and tectonic settings. *Ore Geol. Rev.* **2011**, *43*, 264–293. [CrossRef]
92. Chen, Y.J.; Franco, P.; Lai, Y.; Li, C. Metallogenic time and tectonic setting of the Jiaodong gold province, eastern China. *Acta Pet. Sin.* **2004**, *20*, 907–922.
93. Zhang, L.; Zhang, R.; Wu, K.; Chen, Y.; Li, C.; Hu, Y.; He, J.; Liang, J.; Sun, W. Late cretaceous granitic magmatism and mineralization in the Yingwuling W-Sn deposit, South China: Constraints from zircon and cassiterite U-Pb geochronology and whole-rock geochemistry. *Ore Geol. Rev.* **2018**, *96*, 115–129. [CrossRef]